

AD-A188 887

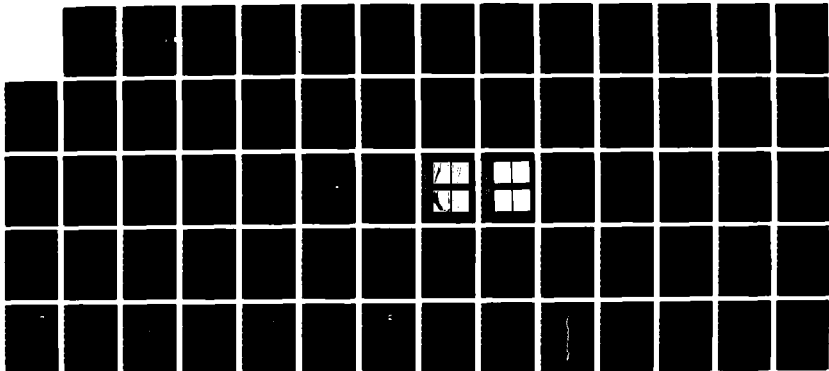
PHOTONIC TEMPERATURE AND PRESSURE SENSORS FOR
BIOSYSTEMS/PULSED MICROWAVE 1 INTERACTION STUDIES(U)
NAVAL RESEARCH LAB WASHINGTON DC A D KERSEY ET AL.
SEP 87

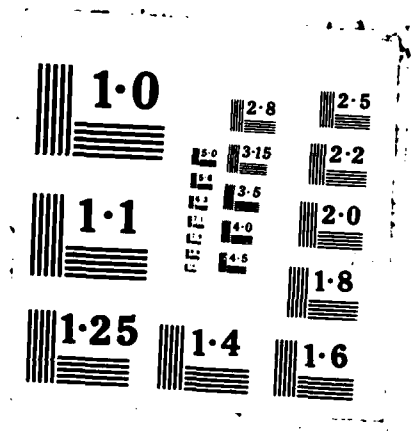
1/1

UNCLASSIFIED

F/G 6/12

NL





AD-A188 887

AD
DTIC FILE COPY

PHOTONIC TEMPERATURE AND PRESSURE SENSORS FOR BIOSYSTEMS/PULSED

MICROWAVE INTERACTION STUDIES

FINAL REPORT

Prepared by

A. D. KERSEY
A. DANDRIDGE
N. LAGAKOS
A. B. TVETEN

SEPTEMBER 1987

Supported by

U.S. ARMY MEDICAL RESEARCH AND DEVELOPMENT COMMAND
Fort Detrick, Frederick, Maryland 21701-5012

Contract No. 85PP5803

U.S. Naval Research Laboratory
Washington, DC 20375-5000

Approved for public release; distribution unlimited

The findings in this report are not to be construed as an official Department of the Army position unless so designated by other authorized documents.

87 12 11 072

DTIC
ELECTE
DEC 30 1987
S D

REPORT DOCUMENTATION PAGE

Form Approved
OMB No. 0704-0188

1a. REPORT SECURITY CLASSIFICATION UNCLASSIFIED		1b. RESTRICTIVE MARKINGS	
2a. SECURITY CLASSIFICATION AUTHORITY		3. DISTRIBUTION / AVAILABILITY OF REPORT Approved for public release; distribution unlimited.	
2b. DECLASSIFICATION / DOWNGRADING SCHEDULE			
4. PERFORMING ORGANIZATION REPORT NUMBER(S)		5. MONITORING ORGANIZATION REPORT NUMBER(S)	
6a. NAME OF PERFORMING ORGANIZATION U.S. Naval Research Laboratory	6b. OFFICE SYMBOL (If applicable)	7a. NAME OF MONITORING ORGANIZATION	
6c. ADDRESS (City, State, and ZIP Code) Washington, DC 20375-5000		7b. ADDRESS (City, State, and ZIP Code)	
8a. NAME OF FUNDING / SPONSORING ORGANIZATION U.S. Army Medical Research & Development Command	8b. OFFICE SYMBOL (If applicable)	9. PROCUREMENT INSTRUMENT IDENTIFICATION NUMBER 85PP5803	
8c. ADDRESS (City, State, and ZIP Code) Fort Detrick Frederick, MD 21701-5012		10. SOURCE OF FUNDING NUMBERS	
		PROGRAM ELEMENT NO. 62777A	PROJECT NO. 3E1 62777A878
		TASK NO. BB	WORK UNIT ACCESSION NO. 012
11. TITLE (Include Security Classification) Photonic Temperature and Pressure Sensors for Biosystems/pulsed Microwave Interaction Studies			
12. PERSONAL AUTHOR(S) A.D. Kersey, A. Dandridge, N. Lagakos, and A.B. Tveten			
13a. TYPE OF REPORT Final	13b. TIME COVERED FROM 10/1/84 TO 9/30/86	14. DATE OF REPORT (Year, Month, Day) 1987 September	15. PAGE COUNT 68
16. SUPPLEMENTARY NOTATION			
17. COSATI CODES		18. SUBJECT TERMS (Continue on reverse if necessary and identify by block number)	
FIELD	GROUP	SUB-GROUP	
06	18		
06	16		
19. ABSTRACT (Continue on reverse if necessary and identify by block number)			
<p>This report details research efforts at the Naval Research Laboratory into the development of miniature, high frequency, optical fiber pressure and temperature sensors for use in monitoring transient pressure and heating in biological samples under microwave irradiation. The first sections of the report describe the various pressure and temperature sensor configurations studied and/or tested experimentally. Section B reports the results obtained with field tested (at Walter Reed) prototype sensors, and Section C describes the operational details and calibration of the temperature and pressure sensor units for delivery to Walter Reed.</p>			
20. DISTRIBUTION / AVAILABILITY OF ABSTRACT <input type="checkbox"/> UNCLASSIFIED / UNLIMITED <input checked="" type="checkbox"/> SAME AS RPT. <input type="checkbox"/> DTIC USERS		21. ABSTRACT SECURITY CLASSIFICATION Unclassified	
22a. NAME OF RESPONSIBLE INDIVIDUAL Mary Frances Bostian		22b. TELEPHONE (Include Area Code) 301-663-7325	22c. OFFICE SYMBOL SGRD-RMI-S

SECTION A

1. Pressure Sensors

Two approaches to the development of a miniature fiber optic pressure sensor have been considered in this project. These comprise systems based on interferometric techniques for the measurement of a) pressure induced displacements of a miniature diaphragm arrangement, and b) direct pressure induced optical path length variations in pre-sensitized optical fiber sections (coil sensor).

1.1 Diaphragm Sensor

The measurement of small pressure induced displacements in a diaphragm can be accomplished with extremely high sensitivity utilizing optical interferometry. Figure A.1 shows a diagram of the proposed pressure sensor based on the use of a fiber optic Michelson interferometer and a miniature reflective diaphragm arrangement. Light in one arm of the interferometer is reflected back towards the coupler by reflection off the rear of the pressure sensing diaphragm. By ensuring that the cleaved end of the sensing fiber is positioned close to the diaphragm, a fraction of the uncollimated light emanating from the fiber can be



Admission For	
DTIC CRA&I	<input checked="" type="checkbox"/>
DTIC TAB	<input type="checkbox"/>
Unannounced	<input type="checkbox"/>
Justification	
By _____	
Distribution /	
Availability /	
Date	Availability of
A-1	Source

recoupled back into the fiber core. This reflected light is guided to the directional coupler and mixes with light which is returned in the reference arm. By monitoring changes in the interference fringe obtained at the output, small changes in the position of the diaphragm can be determined.

It can be shown that the displacement, d , of a diaphragm of radius, a , clamped rigidly along its circumference is, for $d \ll a$, proportional to the applied differential pressure, δP and is given by

$$d = S \frac{\delta P a^4}{Et^3} \quad (1)$$

where t is the thickness of the diaphragm, E its modulus of elasticity, and S is a constant depending on the load distribution applied to the diaphragm. With a uniform load distribution (uniform pressure) $S \approx 0.15$. For a pressure probe of radius, $a = 0.5$ mm, and a diaphragm thickness, $t = 30$ μm , the above equation yields a sensitivity (with E in units of N/m^2)

$$\frac{\delta d}{\delta P} \approx 3.10^{-1}/E \text{ m/Pa} \quad (2)$$

For $E \sim 3.10^8 \text{ Nm}^2$, the displacement sensitivity is

$$\frac{\delta d}{\delta P} \sim 1 \text{ nm/Pa} \quad (3)$$

In the Michelson interferometer configuration this gives rise to an optical phase shift per unit change in pressure, $\Delta\phi$, of

$$\Delta\phi = \frac{4\pi}{\lambda} \frac{\delta d}{\delta P} \text{ rad/Pa.} \quad (4)$$

For a HeNe laser source, $\lambda = 633$ nm and

$$\Delta\phi \approx 0.02 \text{ rad/Pa.} \quad (5)$$

The minimum detectable phase shift, $\Delta\phi_{\text{min}}$, in a single mode fiber

interferometer, is typically $\sim 10^{-6}$ rad/Hz^{1/2} over the range 10 Hz to 100 kHz. This phase shift detection sensitivity corresponds to a minimum pressure detectability of

$$\begin{aligned} \delta P_{\min} &\sim 5.10^{-5} \text{ Pa/Hz}^{1/2}, \\ \text{i.e.} &\sim 50 \text{ } \mu\text{Pa/Hz}^{1/2}. \end{aligned} \tag{6}$$

For application in biological systems, it is crucial that the dynamic range of the sensor be sufficient to allow small (i.e., \sim mPa) variations in pressure to be detected above a quasi-static background level of $\sim 10^4$ Pa (\approx 100 mm Hg). This background pressure produces a large displacement of the diaphragm and determines the minimum proximity of the fiber end and the diaphragm. In order to maintain a linear dependence between applied pressure and optical phase shift, the displacement due to the background pressure should satisfy $d_{\max} \ll a$. For the dimensions of the probe proposed here, the diaphragm displacement at a pressure of 10^4 Pa is $\approx 10 \text{ } \mu\text{m}$, which adequately satisfies the above condition.

The fundamental resonant frequency of this device is dependent primarily on the mass of and the tension in the diaphragm. Typically, a device could be tailored to provide a flat response up to a frequency of ~ 10 kHz with a fundamental resonance in the 20-50 kHz region.

1.2. Coil Sensor

In this sensor pressure induces directly optical path length variations in a single mode fiber which are detected by using a Mach-Zehnder interferometer. Below the analysis is given first and then the experimental results.

1.2.1. Pressure Sensitivity of Optical Fibers (Analysis)

The pressure sensitivity of the optical phase in a fiber is defined as $\Delta\phi/\phi\Delta P$, where $\Delta\phi$ is the shift in the phase ϕ due to a pressure change ΔP . If a

given pressure change ΔP results in a fiber core axial strain ϵ_z and radial strain ϵ_r , it can be shown that

$$\frac{\Delta\phi}{\phi} = \epsilon_z - \frac{n^2}{2} [(P_{11} + P_{12}) \epsilon_r + P_{12} \epsilon_z] \quad (7)$$

Here, P_{11} and P_{12} are the elastooptic or Pockels coefficients of the core, and n is the refractive index of the core. The first term in Eq. (7) is the part of $\Delta\phi/\phi\Delta P$ which is due to the fiber length change, while the second and third terms are the parts due to the refractive-index modulation of the core, which is related to the photoelastic effect¹.

In order to calculate the sensitivity as given in (7), the strains in the core ϵ_z and ϵ_r must be related to the properties of the fiber layers.

The polar stresses σ_r , σ_θ , and σ_z in the fiber are related to the strains ϵ_r , ϵ_θ , and ϵ_z as follows².

$$\begin{bmatrix} \sigma_r^i \\ \sigma_\theta^i \\ \sigma_z^i \end{bmatrix} = \begin{bmatrix} (\lambda^i + 2\mu^i) & \lambda^i & \lambda^i \\ \lambda^i & (\lambda^i + 2\mu^i) & \lambda^i \\ \lambda^i & \lambda^i & (\lambda^i + 2\mu^i) \end{bmatrix} \begin{bmatrix} \epsilon_r^i \\ \epsilon_\theta^i \\ \epsilon_z^i \end{bmatrix}, \quad (8)$$

where i is the layer index (0 for the core, 1 for the cladding, etc.), and λ_i and μ^i are the Lamé parameters² which are related to Young's modulus E^i and Poisson's ratio ν^i as follows:

$$\lambda^i = \frac{\nu^i E^i}{(1 + \nu^i)(1 - 2\nu^i)}, \quad \mu^i = \frac{E^i}{2(1 + \nu^i)}. \quad (9)$$

For a cylinder the strains can be obtained from the Lamé solutions³.

$$\epsilon_r^i = U_o^i + \frac{U_l^i}{r^2}, \quad \epsilon_\theta^i = U_o^i - \frac{U_l^i}{r^2}, \quad \epsilon_z^i = W_o^i, \quad (10)$$

where $U^i/0$, $U^i/1$, and $W^i/0$ are constants to be determined. Since the strains must be finite at the center of the core, $U^0_1 = 0$.

For a fiber with m layers the constants U^i_0 , U^i_1 , and W^i_0 in Eq. (4) are determined from the boundary conditions:

$$\sigma_r^i |_{r=r_i} = \sigma_r^{i+1} |_{r=r_i} \quad (i = 0, 1, \dots, m-1), \quad (11)$$

$$u_r^i |_{r=r_i} = u_r^{i+1} |_{r=r_i} \quad (i = 0, 1, \dots, m-1), \quad (12)$$

$$\sigma_r^m |_{r=r_m} = -P, \quad (13)$$

$$\sum_{i=0}^m \sigma_z^i A_i = -PA_m, \quad (14)$$

$$\epsilon_z^0 = \epsilon_z^1 = \dots = \epsilon_z^m, \quad (15)$$

where $u_r^i (= \int \epsilon_r^i dr)$ is the radial displacement in the i th layer, and r_i and A_i are the radius and the cross-section area of the i th layer, respectively.

Equations (11) and (12) describe the radial stress and displacement continuity across the boundaries of the layers. Equations (13) and (14) assume that the applied pressure is hydrostatic. Equation (15) is the plane strain approximation which ignores end effects. For long thin cylinders such as fibers it introduces an error of less than 1%. Using the boundary conditions described by Eqns. (11) and (12), the constants U^i_0 , U^i_1 , and W^i_0 are determined and ϵ_r^0 and ϵ_z^0 are calculated from Eq. (10). Then, from Eq. (7) the sensitivity $\Delta\sigma/\Delta P$ can be found.

a. Low Frequency Regime (Hydrostatic)

In the low frequency regime (up to several KHz's) the dominant strain is the ϵ_z (Eq. (7)). In this low frequency regime where pressure is hydrostatic,

for fibers with very thick coatings the pressure sensitivity is proportional to the inverse of the bulk modulus of the outer hard polymeric coating⁴. In this case high sensitivities are obtained with low bulk modulus coatings. For fibers with more typical coating thicknesses, the sensitivity becomes a more complicated function of the elastic moduli. In this case the waveguide experiences anisotropic strains and knowledge of two independent elastic moduli is required to predict the acoustic sensitivity. In fibers with thin coatings, the glass part of the fiber becomes important and it will resist to the stresses generated in the coating due to the applied acoustic field. Then, the relevant question is what ratio of these stresses will propagate to the fiber core to modulate the phase. This fraction is governed by the Young's modulus of the coating: the higher the Young's modulus the higher is that ratio⁴. As the thickness of the coating increases, higher stress fraction communicates to the core and the bulk modulus becomes increasingly more dominant parameter.

In conclusion, for typical fibers, high sensitivity is obtained with polymeric coatings having low bulk and high Young's moduli, which increases as the coating thickness increases⁴.

b. High Frequency Regime (Axially Constrained).

For high frequency acoustic fields, initial effects do not permit a net axial strain contribution over the sensing fiber. The length of the fiber is frozen and the acoustic sensitivity is due entirely to the refractive index modulation. In this case, the fiber sensitivity is governed entirely by the radial strain term, ϵ_r , since $\epsilon_z = 0$ (Eq. (7)). In this high frequency regime where the Young's modulus is not expected to play an important role ($\epsilon_z = 0$), the bulk and, to a smaller degree, the shear moduli are the parameters which govern the acoustic sensitivity: the smaller the bulk and shear moduli, the

higher the sensitivity⁵. However, contrary to the hydrostatic case, only moderate increase in sensitivity can be obtained by a proper coating selection.

1.3. Acoustic Response of Fiber Optic Coil Sensor (Experimental)

Different fiber optic sensor designs were studied having cylindrical configurations with constant and varying radius. The final fiber optic sensing element (Fig. A.2) consisted of a planar fiber coil (length of fiber 0.92m) mounted on a nylon annulus of 0.1588 cm thickness, 0.6 cm i.d., and 2.05 cm o.d. The inside fiber loop had a 0.6 cm diameter and the outside loop a 1.85 cm diameter. The fiber was a 0.17 NA single mode fiber consisted of a 80 μm o.d. glass, a 200 μm o.d. silicone, and a 350 μm o.d. nylon. The experimental apparatus used to measure the acoustic response of the fiber coil sensor is shown in Fig. A.3. A single mode He-Ne laser was used as a source, the light beam was coupled into the sensing and reference fibers, and the two beams were finally then recombined and detected by a photomultiplier whose output was read by a spectrum analyzer. The fiber coil sensor was immersed into a 43 cm x 45 cm x 10 cm (height) tank filled with water. The acoustic field was generated by PZT transducers which were placed 10 cm away from the fiber coil. Very close to the fiber coil a small LC-5 probe was used to monitor the acoustic pressure of the PZT transducer. Three PZT transducers were used having peak output at 0.5 MHz, 1 MHz, and 2.25 MHz to study the acoustic response of the fiber coil sensor from 150 KHz to 3.7 MHz. Figs. A.4 and A.5 show the acoustic response of the fiber coil and the response of the LC-5 (smoother curve). Since the response of LC-5 is not flat for frequencies higher than 200 KHz (Fig. A.6), a PVF₂ probe with flat frequency response was used to calibrate the LC-5 at high frequencies (Fig. A.7). From this calibration and the responses of the fiber coil and LC-5 (Figs. A.4 and A.5) the acoustic response of the fiber coil sensor was obtained

and it is shown in Fig. A.8. In Fig. A.8 it is also indicated the analytically obtained sensitivity using Eq. 7. The response of the fiber coil is not flat, contrary to the analytical predictions, indicating the existence of a broad resonance peak at lower frequencies. The small peaks at ~ 0.8 MHz and ~ 2.4 MHz are due to the $\lambda/2$ and $3\lambda/2$ resonances of the nylon backing disk.

Pulse response. The response of the fiber coil sensor was also studied using the 0.5 MHz PZT transducer which was excited using a pulse generator (Fig. A.9). The pulse was generated by a 8013B Hewlett Packard pulse generator used together with a 3310B Hewlett-Packard function generator whose output was amplified by a RF (EIN 240 L model) power amplifier which drove the 0.5 MHz transducer. The acoustic response was the expected one (Fig. A.9), and no low frequency ringing was observed in these experiments.

2. Temperature Sensor

2.1. Introduction

Optical fiber sensors offer unique advantages over conventional sensors for the measurement of temperature in a variety of applications where the sensor is subjected to high RFI/EMI or is operated in hazardous environments. Consequently, a number of sensor types have been developed in recent years for use in biomedical and industrial applications. In the former case, the EMI immunity and bio-compatibility of optical fiber sensors make them ideal candidates for temperature monitoring in cancer treatment by RF or microwave radiation induced hyperthermia. In the industrial area, fiber optic sensors can be used to monitor temperature in chemical plants, furnaces, nuclear reactors, etc.

In general, fiber optic temperature sensors can be classified as either intrinsic or extrinsic. In intrinsic sensors types, the 'sensing element' is

formed by the optical fiber itself. Several sensors have been developed which fall into this category; for example, using a thermosensitive cladding [6,7], using a Michelson or Fabry-Perot Interferometer [8,9], or by doping the fiber core using a rare earth element [10]. Extrinsic sensors on the other hand, use the optical fiber merely as a 'light-pipe' to convey optical power to and from an external 'sensing element' which modulates the transmitted or reflected light. In this case, the external sensing element can be formed using phosphors, birefringent crystals, semiconductors, liquid crystals, thermochromic materials, etc., which modulate either the fluorescence intensity decay, direct intensity, or wavelength (or wavelength distribution, i.e., color) of the returned light with changing temperature.

The advantages/disadvantages of each of these techniques vary depending on the exact sensing mechanism. For example, some offer extremely high resolution but are not absolute, whereas others may offer high accuracy over a small range. In each case, however, a finite thermal response time is involved which arises due to the time required for either the fiber or external sensing material to equilibrate with the surrounding temperature. This is very dependent on the exact design of the sensor, but is typically in the range of 10 ms to several hundred ms.

Direct optical probing of the medium of interest using optical fiber offers a means of overcoming this thermal time constant effect inherent to most other fiber-optic temperature sensors. Temperature sensing by direct optical probing of a medium is based on detecting the change in refractive index of a material with temperature. As the refractive index of a medium changes, the optical reflection coefficient at the interface between the fiber (typically silica) and the medium changes according to the Fresnel reflection formulae [11].

Temperature variations can thus be monitored by measuring the fractional intensity of light reflected from such an interface. In the particular case of pure water in study here, this effect is reasonably strong ($dn/dT \sim 10^{-4} \text{ }^\circ\text{C}^{-1}$ in the region 25-30 $^\circ\text{C}$, see Figure A.10) and can be used to provide direct monitoring of transient temperature changes in a sample. Due to the technical difficulty in obtaining stable reflection over a long time period, however, the technique is not suitable for absolute temperature monitoring.

Two basic 'direct optical-probing' approaches to monitor temperature induced changes in refractive index can be used based on a) Near Total Internal Reflection (NTIR) or b) Normal Incidence Reflection (NIR). Sensor designs based on these methods are described in the following sections.

2.2. Near total-internal-reflection (NTIR) temperature sensor.

The optical fiber NTIR temperature sensor is a simple, direct interaction, optical probe in which the 'effective reflectance' of the probe tip is monitored as a function of the temperature of the medium external to the fiber. A high reflection coefficient at the sensing end of the fiber is achieved by polishing the fiber close to, but less than, the critical angle for the fiber-external medium interface. As shown in the diagram of Fig. A.11.a, a second fiber end-face cut with a reflecting coating is also required to reflect the light from the NTIR interface back towards the fiber core (via a second NTIR interface reflection). The intensity of light returned along the fiber can be monitored using a fiber directional coupler, and referenced directly to the source intensity, as shown in Fig. A.11.b. The sensitivity of the technique depends strongly on how well the device can be 'biased,' which is determined by the angular precision with which the fiber end face can be cut and polished. The Fresnel reflectivity curve for an interface between quartz ($n = 1.54$) and

pure water (Fig. A.12) at a wavelength of $\sim 0.6 \mu\text{m}$, is shown by the solid line in Fig. A.13. The reflection coefficient is given by [11]

$$r = \left\{ \frac{\tan(\phi_i - \phi_r)^2}{\tan(\phi_i \phi_r)} \right\} \quad , \quad (A)$$

where ϕ_i and ϕ_r are the angles of incidence (defined by the interface angle) and refraction, with ϕ_r given by

$$\phi_r = \sin^{-1} \left\{ \frac{n_o}{n_e} \sin \phi_i \right\} \quad . \quad (B)$$

and n_o and n_e are the refractive indices of the silica and water. In Figure A.13 the curve depicts the reflectivity of a plane interface at an angle of incidence of 59.5° , which corresponds to the critical angle for the quartz-water interface at a temperature of 39.5°C ($n_e = 1.330$). With a dn/dT for pure water of approximately $-10^{-4}^\circ\text{C}^{-1}$ (Fig. 2.1) the reflectivity of the interface is found to decrease when the temperature drops below the temperature, T_c , at which total internal reflection is first attained. It can be seen that the sensitivity of the technique becomes arbitrarily large when the 'critical temperature' T_c , is approached; however, due to the nonlinear response, the range over which a high sensitivity can be achieved is limited. At temperatures significantly lower than the T_c a near constant, but substantially reduced sensitivity may be obtained over an appreciable temperature range.

The open circles and broken curve in Figure A.13 shows the experimentally observed change in reflectance of a quartz-water interface with decreasing temperature. The smearing of the response curve near the critical temperature is due to the finite divergence of the HeNe laser beam used in the determination

of the interface reflectance. The sensitivity displayed by this curve varies between $1\%^{\circ}\text{C}^{-1}$ at $\sim 25^{\circ}\text{C}$ to $\sim 3\%^{\circ}\text{C}^{-1}$ at 35°C .

In the fiber NTIR probe shown in Figure A.11.a two NTIR interface reflections are involved (i.e., effective probe reflectivity, $R = r^2$), thus doubling the intrinsic sensitivity of the technique. Theoretical response curves for a fused silica fiber water interface are shown in Figure A.14 for two fiber end face angles; (a) -66.23 and (b) 66.0° (measured relative to a normal (perpendicular) end face). Here it can be seen that the sensitivity depends strongly on the bias angle (fiber end face), and two basic modes of operation are possible which give rise to either a high sensitivity with a low working range, or a lower sensitivity with a larger range. Two such ranges are depicted in Figure A.14. In region A, a linear range of $\sim 20^{\circ}\text{C}$ can be achieved with sensitivity (dR/dT) of $\sim 0.25\%/^{\circ}\text{C}$, whereas in region B, an approximately linear response can be obtained from ~ 50 to 55°C with a sensitivity of $\sim 3\%/^{\circ}\text{C}$. As the two curves represent the response functions for end face angles separated by ~ 15 min of arc, it is clear that a high degree of angular precision would be required to implement this approach. This requirement is a major drawback of the NTIR probe design.

2.3. Normal Interface Reflection (NIR) Temperature Sensor

In order to avoid the necessity for accurately polishing the fiber end face, a simpler probe design based on the change in reflectance at a normal incidence interface (Figure A.15) was investigated. In this case, the end face reflectivity is defined simply by the well known Frensel equations for normal incidence, i.e.,

$$R = \left\{ \frac{n_o - n_e}{n_o + n_e} \right\}^2 \quad (C)$$

The theoretical response curve for a fused silica-water interface is shown in Figure A.16, where it can be seen that the absolute reflectance is much lower (~ 0.2%). A significant increase in reflectance with temperature is obtained, however, over the range shown. The figure of merit which allows the responsivity of the NIR and NTIR approaches to be compared is

$$S_r = \frac{1}{R} \frac{dR}{dT} , \quad (D)$$

which defines the fractional change in returned power/unit change in temperature. Comparing Figures A.14 and A.16 it can be seen that the normalized responsivity is only a factor x6 reduced for the NIR approach (at ~ 25°C) over that obtained with a NTIR probe biased at 66.0° ($S_r = 3.10^{-3} \text{°C}^{-1}$ and 2.10^{-2}°C^{-1} , respectively). Considering the fact that the NIR approach does not involve a precisely angled polish of the fiber end face, this reduction in responsivity is not a major disadvantage, and the simplicity of the approach is attractive. Figure A.17 shows the variation in dR/dT for this probe design and indicates that the responsivity increases steadily with temperature, doubling in magnitude over the range 15 to 55°C.

Figure A.18 shows the measured change in optical power reflected from a normally cleaved fiber end immersed in water, as a function of temperature (measured using a thermocouple). The curves display a more linear relationship than would be expected from Figure A.16, which can be explained in part by the weaker temperature dependence of the fiber refractive index (~ 10 ppm/°C in this temperature range) which is ignored in Figures A.16 and A.17, but can be expected to reduce the responsivity at higher temperatures. Figure A.19 shows a calibration of the probe responsivity in the range 25°C → 30°C. This calibration was performed by measuring the returned power from a NIR probe

switched between two water samples at close but different temperatures. The measured calibration is

$$R_{25-30^{\circ}\text{C}} \sim \frac{.0066}{3.4} = 0.195 (\pm .01)\% , \quad (\text{E})$$

which is in excellent agreement with the value predicted from Figure A.16.

2.4. Alternative Probe Design

One major drawback of direct optical probing technique discussed here is the sensor specificity. This can be overcome by coating the NTIR or NIR interface with a suitable material to produce a non-specific probe. We have studied this approach and identified co-polymer coatings which could be utilized. The NTIR and NIR probe designs would then be as shown in Figure A.20. An example of a suitable coating is Teflon, which exhibits a (dn/dT) of coefficient of approximately 60% that of water in the temperature range $\sim 25^{\circ}\text{C}$. Further work is required to identify other materials with higher (dn/dT) coefficients to increase the sensor responsivity, and to test the feasibility of bonding such materials to the filter end face.

2.5. Discussion

By comparison of the theoretical response curves for the NTIR and NIR probes shown in Figures A.14 and A.16 respectively, it can be seen that for a certain input optical power the returned power level from the NTIR probe should be approximately two orders of magnitude greater than that from the NIR design. Based on shot noise limited performance alone, this means that the NTIR resolution would be higher than that achievable using the NIR approach. Typical estimates for the shot noise performance are; as follows:

- i) NTIR: Assuming a moderate normalized responsivity (Region A in

Figure A.14) of $\sim 2 \cdot 10^{-2} \text{ } ^\circ\text{C}^{-1}/^\circ\text{C}$ ($R \sim 20\%$), and a probe power of $\sim 100 \text{ } \mu\text{W}$, the shot noise limited S/N at the detector is $\sim 4 \cdot 10^6/\sqrt{\text{Hz}}$ which gives rise to a temperature equivalent noise.

$$\begin{aligned} \frac{\Delta T}{\text{Shot Noise}}^{\text{NTIR}} &\approx \frac{1}{2 \cdot 10^{-2} \cdot 4 \cdot 10^6} \text{ } ^\circ\text{C}/\sqrt{\text{Hz}} \\ &= 1.3 \cdot 10^{-5} \text{ } ^\circ\text{C}/\sqrt{\text{Hz}} \end{aligned}$$

or $0.4 \text{ m}^\circ\text{C}$ in a $/\text{kHz}$ b.w.

ii) NIR: Again, assuming a probe power of $\sim 100 \text{ } \mu\text{W}$, a bias reflectance of $\sim 0.2\%$ and a normalized responsivity of $\sim 3 \cdot 10^{-3} \text{ } ^\circ\text{C}^{-1}$, the S/N due to shot-noise at the detector is $\sim 4 \cdot 10^5$, which gives a temperature equivalent noise

$$\begin{aligned} \frac{\Delta T}{\text{Shot Noise}}^{\text{NIR}} &\approx \frac{1}{3 \cdot 10^{-3} \cdot 4 \cdot 10^5} \text{ } ^\circ\text{C}/\sqrt{\text{Hz}} \\ &= 0.8 \text{ m}^\circ\text{C}/\sqrt{\text{Hz}} \end{aligned}$$

or $25 \text{ m}^\circ\text{C}$ in a 1kHz b.w.

From these calculations, the NTIR approach is significantly more attractive due to its higher resolution. In practice, however, it was found to be difficult to achieve high reflectivity with a polished NTIR probe. This was attributed to optical loss factors which are either inherent to the probe design, or arise due to certain practical limitations of the grinding/polishing apparatus used. These limitations are discussed below:

a) Intrinsic loss.

In the NTIR probe design of Figure A.11.b, the image of the fiber core

formed in the three-stage reflection (NTIR interface-mirror surface-NTIR interface) is separated from the core by approximately one half to a full radius of the fiber, depending on the exact geometry used. This separation of the core and its image can give rise to up to ~ 3 dB loss in optical power [12].

b) Angular misalignment.

Due to the large effective separation of the core and its image angular misalignment becomes a critical factor in the performance of the probe. In the NTIR design, two flats have to be polished, which each have to be aligned in two planes. If the accuracy with which the flats can be polished is $\sim \pm 0.5^\circ$ then the net angular error can be as great as $\pm 2^\circ$ (considering the three reflections which occur). As the acceptance core of the fiber, which is defined by the fiber numerical aperture (N.A. ~ 0.1 to 0.15 for most single-mode fibers) is $\sim \pm 6^\circ$. Clearly, a possible error of $\pm 2^\circ$ can lead to a large excess loss factor, and combined with the effective core separation, this angular misalignment can lead to excess loss >10 dB (estimated by extrapolation of the results of Ref. 12). Consequently, the effective probe reflectance can be reduced by more than an order of magnitude. This was observed in practice, as the maximum effective NTIR probe reflectance achieved with the device in air (total internal reflection) was $\sim 4\%$. Consequently the maximum achievable shot noise sensitivity would be a factor ~ 5 worse than that predicted above. As these excess loss factors do not arise in the case of the NIR probe, the shot-noise limited temperature detection sensitivity achievable in practice would be only a factor less than 10 lower for the NIR approach compared to the NTIR.

Considering the technical problems associated with the construction of the NTIR probe, and the excess loss factors discussed above, we opted to base the prototype sensor on the NIR design.

3. Summary

This section has discussed the various approaches investigated for the development of miniature fiber-optic pressure and temperature sensors high frequency operation.

Testing of prototype pressure and temperature sensors at Walter Reed is reported in Section B. Details of the deliverable sensor units are given in Section C.

SECTION B

Testing of sensor prototypes at Walter Reed.

1. Pressure Sensor.

The spiral fiber acoustic sensor element described in Section A (Fig. A.2) was incorporated into a Mach-Zehnder (M.Z.) interferometer and configured to monitor pulsed-microwave induced pressure transients in a water chamber situated on a microwave waveguide, as shown in Figure B.1. The laser diode used in these experiments was an Ortel single longitudinal mode 820 nm laser, and photodetection was accomplished using a high-speed EG&G Si pin diode/amplifier hybrid detector. The M.Z. interferometer was unbalanced (~ 3 cm) such that the operating position of the system on the cosine output interference fringe could be adjusted to provide a linear output response (see Figure B.2.). At this operating point, pressure induced optical phase shifts in the interferometer are, to a good approximation, converted linearly into an intensity variation at the detector.

Figure B.3. shows the resulting pressure variation detected with the fiber optic sensor when the water sample was treated with a microwave pulse of 10 μ s duration. Three predominant components are observed in the output: (a) a step (offset) in the mean output level, (b) a transient increase in the output

period of several hundred milliseconds), (b) an oscillatory component at ~ 33 KHz, and a secondary and weaker oscillatory component at ~ 5 KHz. These components in the detected interferometer output intensity correspond to:

a) a step change in the pressure or temperature of the water sample (the probe as presently configured is also sensitive to temperature). The sharp change in mean level ($<100 \mu\text{s}$) indicates that the effect is not due to heating of the water, but probably direct microwave heating of the fibers.

b) a high frequency ringing in the pressure due to an acoustic standing wave between the vertical walls of the tube induced by the transient pressure change.

c) a lower frequency and weaker ringing in the pressure resulting from a vertical resonant mode of the sample chamber.

Figure B.4. shows the result obtained when the vertical walls of the chamber were lined with an open cell foam to suppress sidewall reflections. The output again consists of three main components, but the high frequency ringing is strongly damped.

The peak to peak phase shifts in the results of figures B.3. and B.4. correspond to ~ 1 rad and translate into pressure changes of ~ 8 milli Pa, p-p ($\sim .08 \mu\text{bar}$).

2. Temperature Sensor

The set-up used to test the prototype NIR temperature sensor is shown in Figure B.5. The SLD source was operated in a current and temperature stabilized mode to reduce output intensity fluctuations. Light returned from the normally-cleaved fiber end was directed onto an Si photodetector using a directional coupler, amplified using a differential amplifier (to remove the large background intensity) and analyzed using a Nicolet Signal Averager

(Walter Reed). The sensitivity of the sensor was set to $1\text{V}/^\circ\text{C} \pm 5\%$ at $\sim 25^\circ\text{C}$ and was checked by immersing the probe in calibrated water baths at 25°C and 30°C . Figures B.6. and B.7. show the results of direct pulsed microwave induced heating transients in a water sample monitored using the fiber probe. In Figure B.6. the temperature transient observed in the sample over the initial 400 ms is shown. The measurement time constant here is 2.5 ms., and the temperature step is seen to occur within the response time of the detection electronics. The step in output voltage (mean to mean) was 0.176 V, corresponding to a temperature rise of $0.176 \pm .01^\circ\text{C}$. The standard deviation on the noise (effective rms) is equivalent to 0.027°C , or 0.003°C (3 milli $^\circ\text{C}$) normalized to a 1 Hz b.w. This result is in close agreement to the shot-noise level of ~ 1 milli $^\circ\text{C}$, predicted in Section A(2.5.). The excess noise is attributed to detector thermal noise and amplifier noise. It should be noted that the step change in Figure B.6. corresponds to a light level change at the photodetector of only ~ 25 pW. This is an extremely small increase, and a very large amplification ($\sim 2 \cdot 10^{10}$;) was required to provide signal levels sufficient to interface with the Walter Reed Data Acquisition Equipment. Excess amplifier noise is, therefore, not surprising, and less extreme output scale factor requirements (i.e., 10 mV/ $^\circ\text{C}$) would probably reduce the noise component due to amplification. Figure B.7. shows the monitored temperature rise over a period of approximately 7 seconds after the microwave pulse irradiation of the water sample. Here the measurement time constant is 100 ms, and the step change in temperature calculated from the $1\text{V}/^\circ\text{C}$ sensor scale factor is 0.18°C , in agreement with Figure B.6. The time constant of the temperature decay, which is governed by heat loss due to thermal conductivity/convection is ~ 5 seconds.

SECTION C

Delivered Sensor Units

1. Pressure Sensor

Figure C.1 shows a schematic block diagram of the miniature fiber-optic pressure sensor. The source, detector and demodulation electronics are housed in a line-powered module which provides an output scale factor of 1V/radian. The fiber Mach-Zehnder pressure sensor with the spiral sensing element is connected to the signal processing module via two fiber leads.

Figure C.2 shows a schematic of the demodulation electronics. To achieve high frequency operation, the system is maintained at quadrature using direct feedback to the laser emission frequency, and phase shift information is extracted directly from the photodetector output. In order to achieve a constant scale factor, a pilot tone calibration technique is incorporated which allows the scale factor of the demodulator to be set before each measurement. The system frequency response is 10 Hz ~ MHz with a dynamic range of 10^5 .

Full details of the operation, calibration of the miniature fiber-optic pressure sensor will accompany the delivered unit (scheduled for fall '87).

2. Temperature Sensor.

2.1. Description

A schematic block diagram of the optical fiber NIT temperature sensor is shown in Figure C3. The unit employs a General Optronics GO-DIP 3000 super radiant diode as the optical source. This device has a short coherence length (broadband, see Figure C.4.), and is capable of providing up to 500 μ w of optical output power into a single mode optical fiber pigtail. The source is operated in a current and temperature stabilized mode using external control circuitry. Injection current for the diode is derived from an external,

rechargeable Ni-Cd battery supply. Light from the source is coupled to a 2x2 fiber directional coupler (Amphenol Corp.), which splits the light into two fiber legs. One of these is terminated using an optical mode sink to avoid back reflections, and the other is spliced onto an approximately 20 m length of 'lead' fiber. The end of this fiber lead is the NIR sensory probe. Light reflected back from the probe passes back through the directional coupler to an Si photodetector. The resulting photocurrent is amplified using a transimpedance amplifier. The large background level is then removed using a differential amplifier so that small changes in the reflected intensity due to temperature changes at the NIR can be amplified and monitored. The final stage of amplification provides an adjustable gain which allows the sensor scale-factor to be set. The present system is designed to operate with a scale-factor of 100 mV/°C.

The effectiveness of the SLD intensity stabilization circuitry in compensating for source output fluctuations is shown in Figure C.5. Here, trace (a) shows the sensor output over a period of ~ 25 seconds without SLD stabilization. The drift in the output corresponds to ~ 4°C/min. With intensity stabilization, shown by trace (b), the output is stable over the recording period. Figure C.6. shows the drift recorded over a period of 2 mins. It can be seen that the maximum drift is approximately $\pm 0.1^\circ\text{C}$ over this time.

2.2 Sensor specifications and calibration

The following, with reference to Figures C.7. through C.10, outlines the power requirements, operation and calibration of the NIR temperature sensor.

2.2.1. Power Requirements:

- (i) ± 15 V DC GND regulated supply; input 1B
- source; external power supply.
- (ii) - 5 V DC Super-luminescent diode (SLD) supply; input 2B.
- source; SLD power supply/recharger module.
- (iii) + 20 V DC Detector battery charging input; input 8B,
- source; SLD power supply/recharger module. (Note this input draws current only when the sensor module is OFF, and the switch (7B) is in the charge position).

2.2.2. Outputs:

- (i) Meter output, 3B: Voltmeter ranges -
SLD; 1mV 1mA
Cooler; 1mV 1mA
Therm.; Nominally 1V
Cal. set; 2V max
Output; 100 mV/°C (calibrated)
o ; Internal battery test
 > 1V OK
 < 1V recharge.
- (ii) Sensor output 4B: System output - 100mV/°C \pm 10% Calibrated.

2.2.3. Operating Procedure:

- (i) Power on (1) (LED indicator); check internal batteries; set meter select to o. Reading > 1V indicates batteries sufficiently charged.
- (ii) Detector dark current/amplifier offset null; with calibration (8) set to normal and the gain control (9) set to max (fully C.W.) set meter select (7) to Cal. set, and adjust offset (10) to give meter

reading of zero mV.

(iii) SLD Operation;

With meter select (7) set to SLD, switch SLD power (2) on (indicator). The SLD status LED (6) indicator should be green. Using the coarse SLD current controller (4), adjust the meter reading to ~ 150 mV (\approx 150 mA), and use the fine controller (4) to increase the current to ~ 160 mA. At around 160 mA (\pm 2mA) the SLD status LED should turn red - at this transition point switch the SLD intensity stabilization (3) on (indicator). The SLD status LED should extinguish, indicating the SLD current is within the stabilization range.

Note: The cooler status LED (6) should remain green. The system should not be operated if the cooler status LED remains red for periods on excess of 5 seconds.

(iv) Probe Preparation;

Set the meter select (7) to Cal. set, and calibration (8) to aircalibration. Using a razor blade or fiber jacket stripper, remove ~ 2 to 3 cm of nylon jacket from the fiber probe end. Using acetone, remove the soft primary coating from the fiber and cleave the fiber using the universal cleaving tool provided.

Monitor the meter reading; a reading $>$ 1V indicates a fiber cleave of sufficient quality to conduct measurements. Note, the reading should be quite stable - a fluctuating reading most likely indicates a contaminated probe end (i.e. dust, debris). This can usually overcome by rising the probe end face in acetone.

If a meter reading $>$ 1V is not achieved repeat the cleaving

procedure.

(v) Calibration;

Assuming a meter reading $> 1V$ was achieved from the probe preparation, immerse the probe in the water sample, switch the calibration (8) mode to normal and adjust the gain (9) to give a reading of 200 mV (if this cannot be achieved repeat fiber preparation procedure). With the probe in water and the meter adjusted to 200 mV, adjust offset (10) to null the meter reading. Switch meter select (7) to output and readjust offset to give $\sim 0V$. Output responsivity is then set for $100mV/^{\circ}C \pm 10\%$ in the 25° to $30^{\circ}C$ range.

(vi) Check system;

SLD current - $160 mA \pm 5 mA$.

Cooler current - $< 250 mA$.

Thermistor - 9.5 to 10.5 Volts.

2.2.4. LD Power supply/recharger module.

Front Panel:

Mode select (1C): Off, Normal, Charge.

Battery charging indicators, internal (2C), external (3C).

Specifications

Outputs.

(i) SLD output (4C): - 5V DC @ 1A max.

- Caution severe damage may result if this output is short circuited.

(ii) External Ni-Cd Battery charger output (5C): + 26 V DC
@ 25 mA.

Input.

(i) 120 V AC line input (6C), switched (7C) and fuse protected (8C).

References

1. B. Budiansky, D. C. Drucker, G. S. Kino, and J. R. Rice, Appl. Opt. 18, 4085 1979.
2. J. F. Nye, Physical Properties of Crystals (Oxford U.P., New York, 1976).
3. S. P. Timoshenko and J. N. Goudier, Theory of Elasticity (McGraw-Hill, New York, 1970), Chap. 4.
4. N. Lagakos, E.U. Schnaus, J. H. Cole, J. Jarzynski, and J. A. Bucaro, IEEE J. Quantum Electron., Vol. QE-18, p.683, 1982.
5. N. Lagakos, J. H. Cole, and J. A. Bucaro, J. Lightwave Technol., Vol. LT-1, p. 495, 1983.
6. A. M. Scheggi, *et al.*, Proc. 1st Int. OFS London, p. 13, 1983.
7. P. M. Kopera, J. Melinger and V. J. Tekippe, Proc. SPIE Vol. 412, p. 82, 1983.
8. M. Corke, A. D. Kersey and D. A. Jackson, Electron. Lett., 19, p. 471, 1983.
9. A. D. Kersey, D. A. Jackson and M. Corke, Opt. Comm. 45, p. 71, 1983.
10. E. Sentzer, W. W. Morey and W. H. Glenn, Proc. 1st Int. OFS, London, p. 79, 1983.
11. M. Born and E. Wolf, 'Principles of Optics,' Fourth ed., 1970.
12. M. K. Barnoski, 'Fundamentals of Optical Fiber Communications,' 2nd Ed. Academic Press, New York 1981.

FIGURE CAPTIONS - Section A

- Figure A.1: Miniature diaphragm pressure sensor
- a. Probe head;
 - b. Fiber interferometer configuration.
- Figure A.2: Fiber optic coil sensor: Sensing element
- Figure A.3: Experimental setup for interferometric measurement
- Figure A.4: Acoustic response of fiber coil sensor and LC-5
- Figure A.5: Acoustic response of fiber coil sensor and LC-5
- Figure A.6: Frequency response of LC-5
- Figure A.7: Frequency calibration of LC-5
- Figure A.8: Acoustic sensitivity of fiber optic coil sensor
- Figure A.9: Pulse response of fiber optic coil sensor
- Figure A.10: Dependence of the refractive index of pure water on temperature
($\lambda=0.6 \mu\text{m}$)
- Figure A.11: Near total-internal reflection (NTIR) temperature sensor
- Figure A.12: Reflection and refraction at an interface close to the critical angle
- Figure A.13: Response curves for a single NTIR interface
- Figure A.14: Theoretical response curves for the NTIR probe shown in Figure A.11 for two interface angles
- Figure A.15: Normal incidence reflection (NIR) temperature sensor configuration
- Figure A.16: Theoretical curve showing NIR probe reflectance vs. temperature
- Figure A.17: Change in NIR probe reflectivity vs. temperature
- Figure A.18: Experimentally observed change in reflected intensity from a NIR probe immersed in water as a function of temperature (cooling)

Figure A.19: Calibration of NIR probe reflectance in water at temperatures of 26.2°C and 29.6°C. (Note with probe in air reflectance increase ~ x 20)

Figure A.20: Alternative NTIR and NIR probe designs based on a coated interface

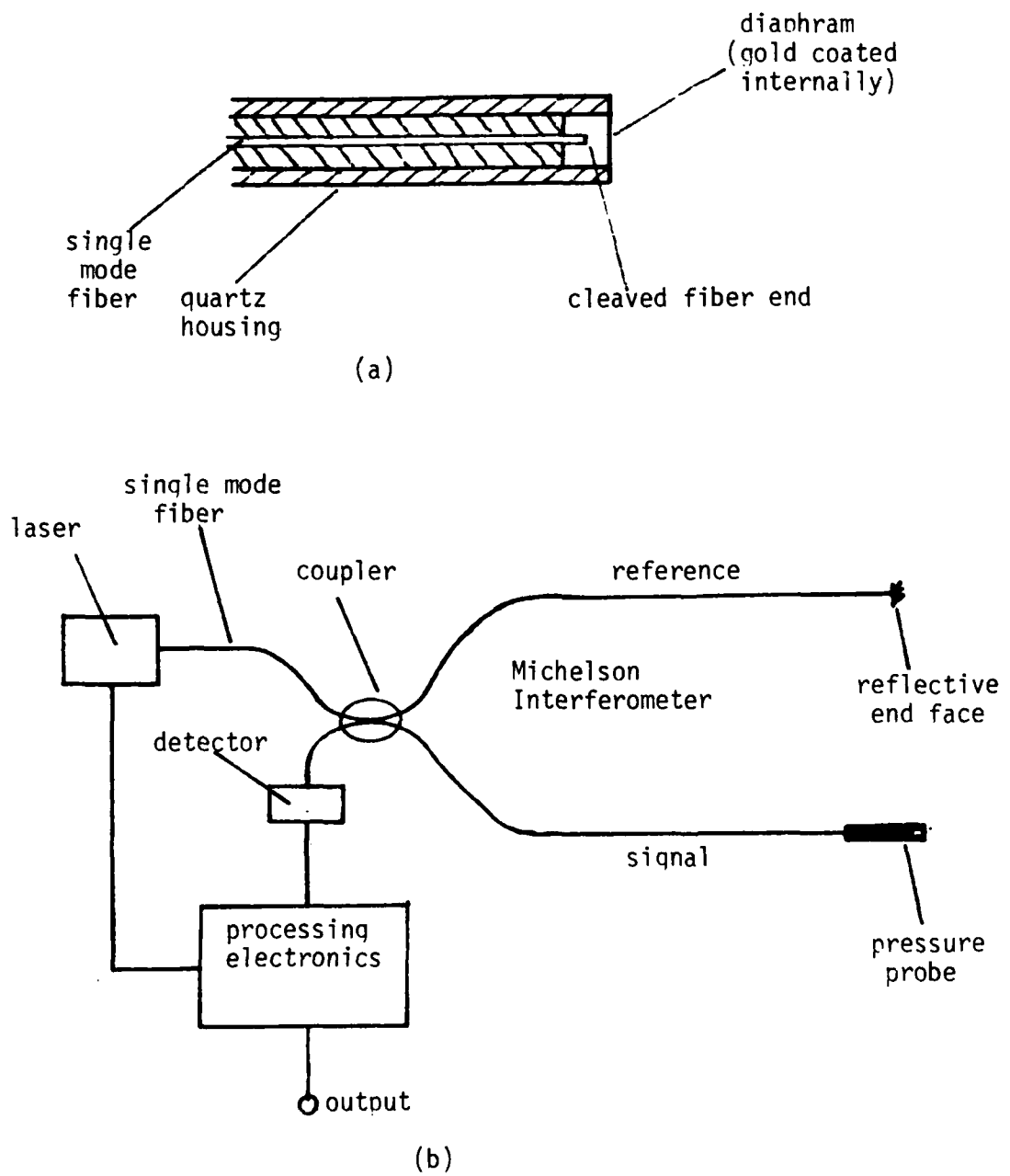


FIGURE A1
 Figure Miniature diaphragm pressure sensor;
 (a) Probe head
 (b) Fiber interferometer configuration.

Fiber Optic Pressure Sensor

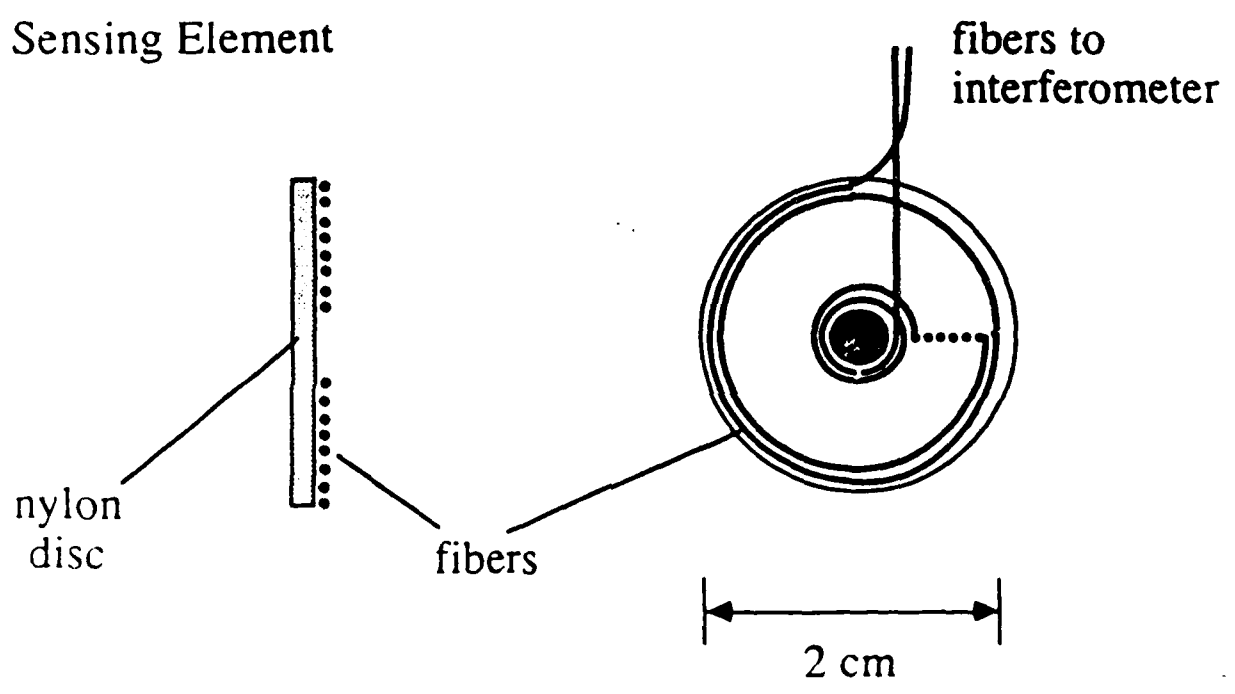


FIGURE A2

EXPERIMENTAL SET UP FOR INTERFEROMETRIC MEASUREMENT

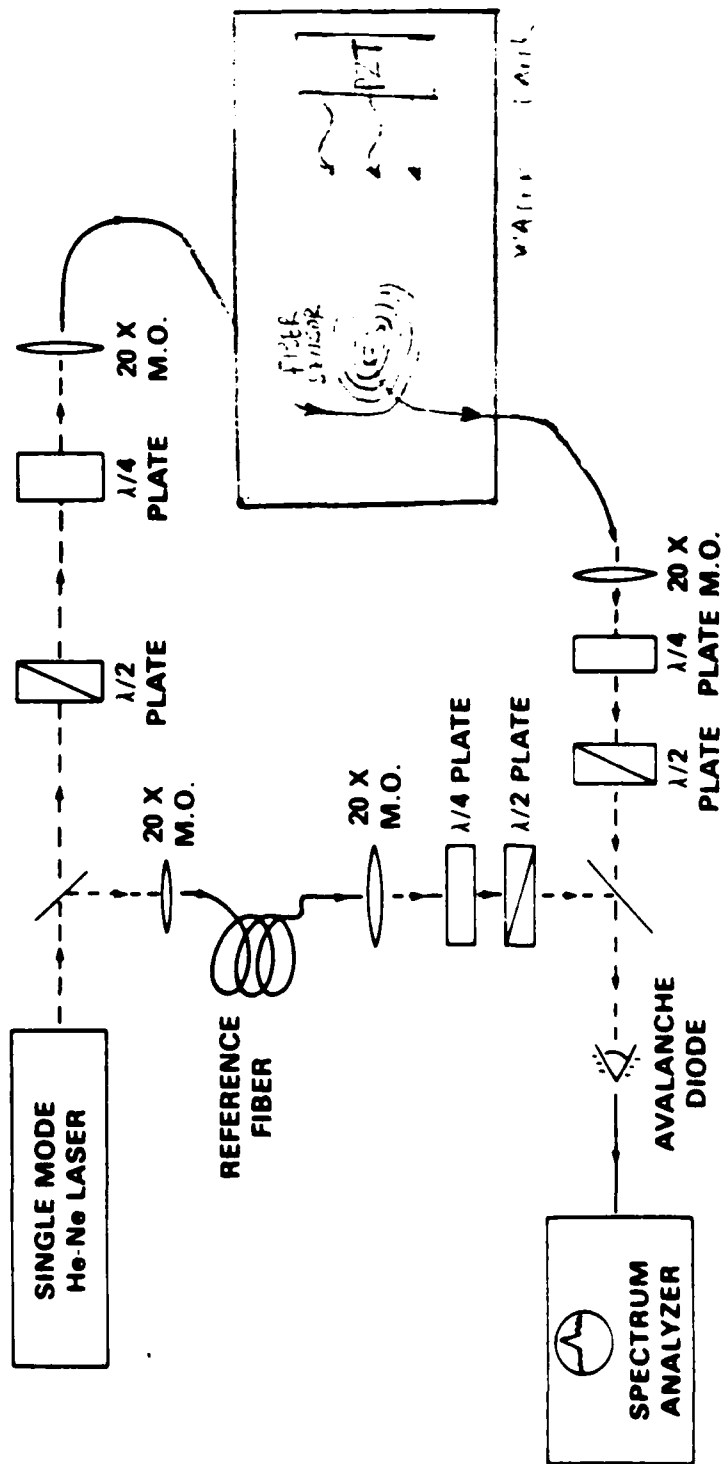


FIGURE A3

ACOUSTIC RESPONSE OF FIBER SENSOR AND LC-5

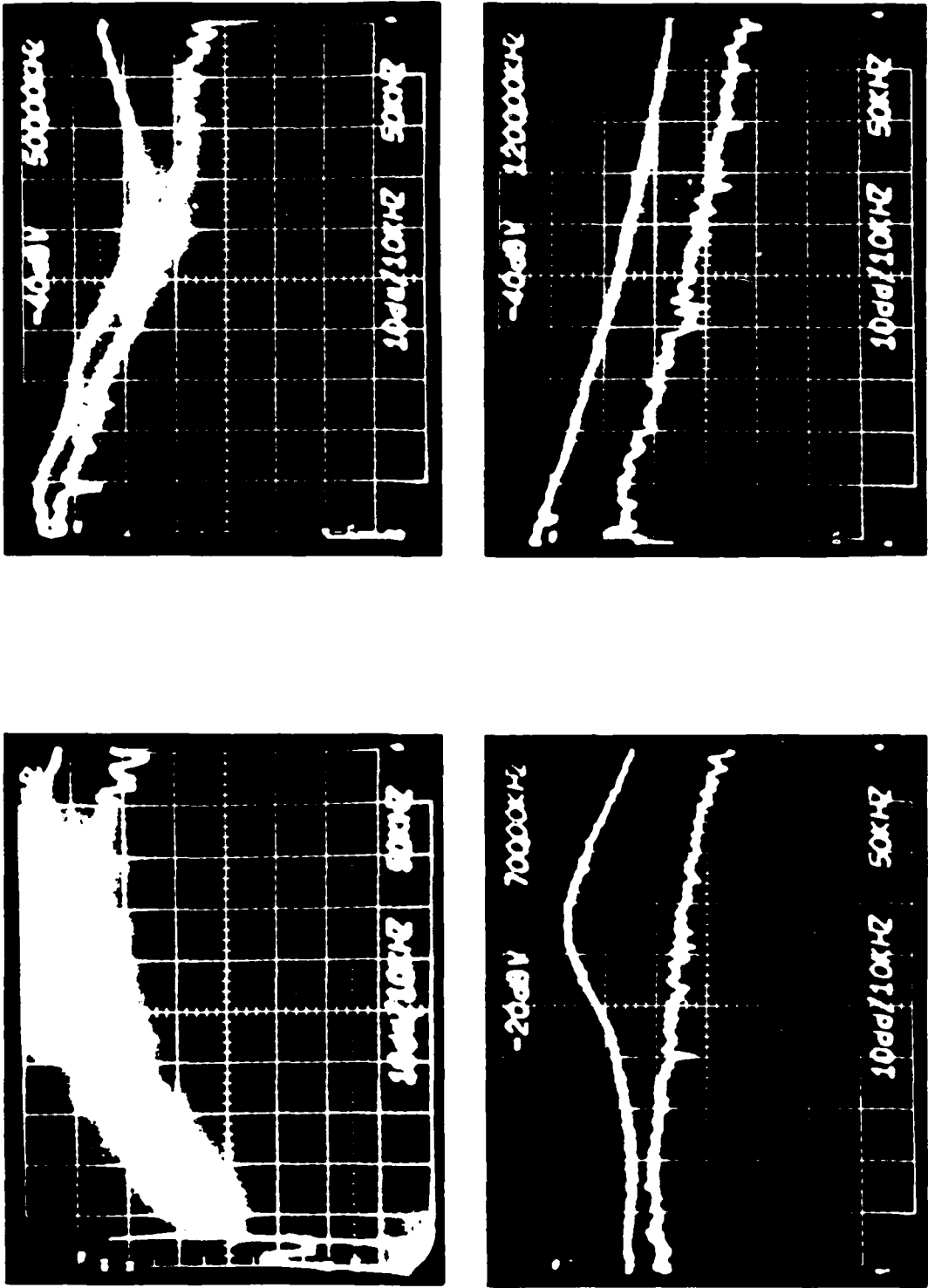


FIGURE A4

ACOUSTIC RESPONSE OF FIBER SENSOR AND LC-5

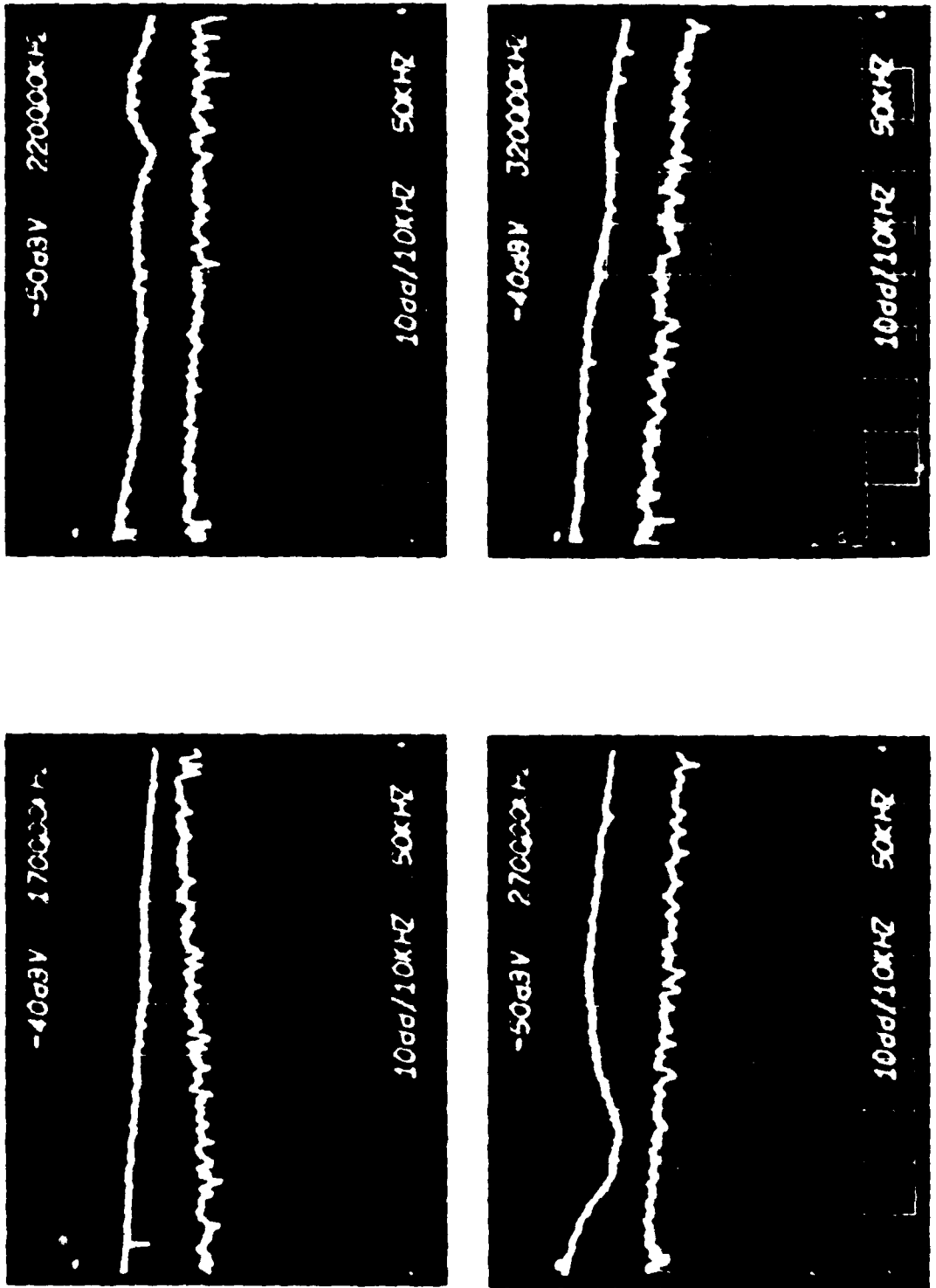


FIGURE A5

FREQUENCY RESPONSE OF LC-5

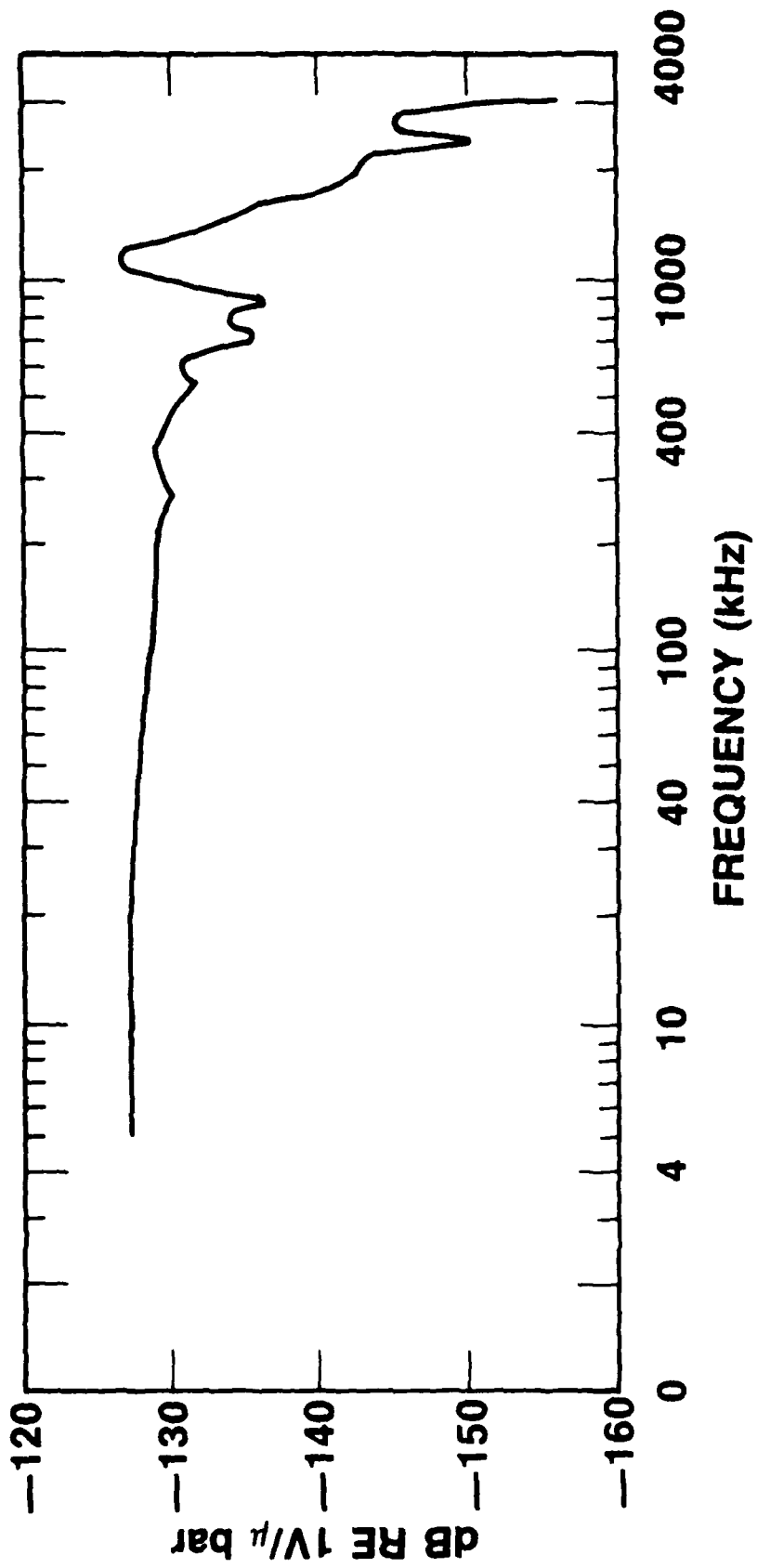


FIGURE A6

FREQUENCY RESPONSE OF LC-5

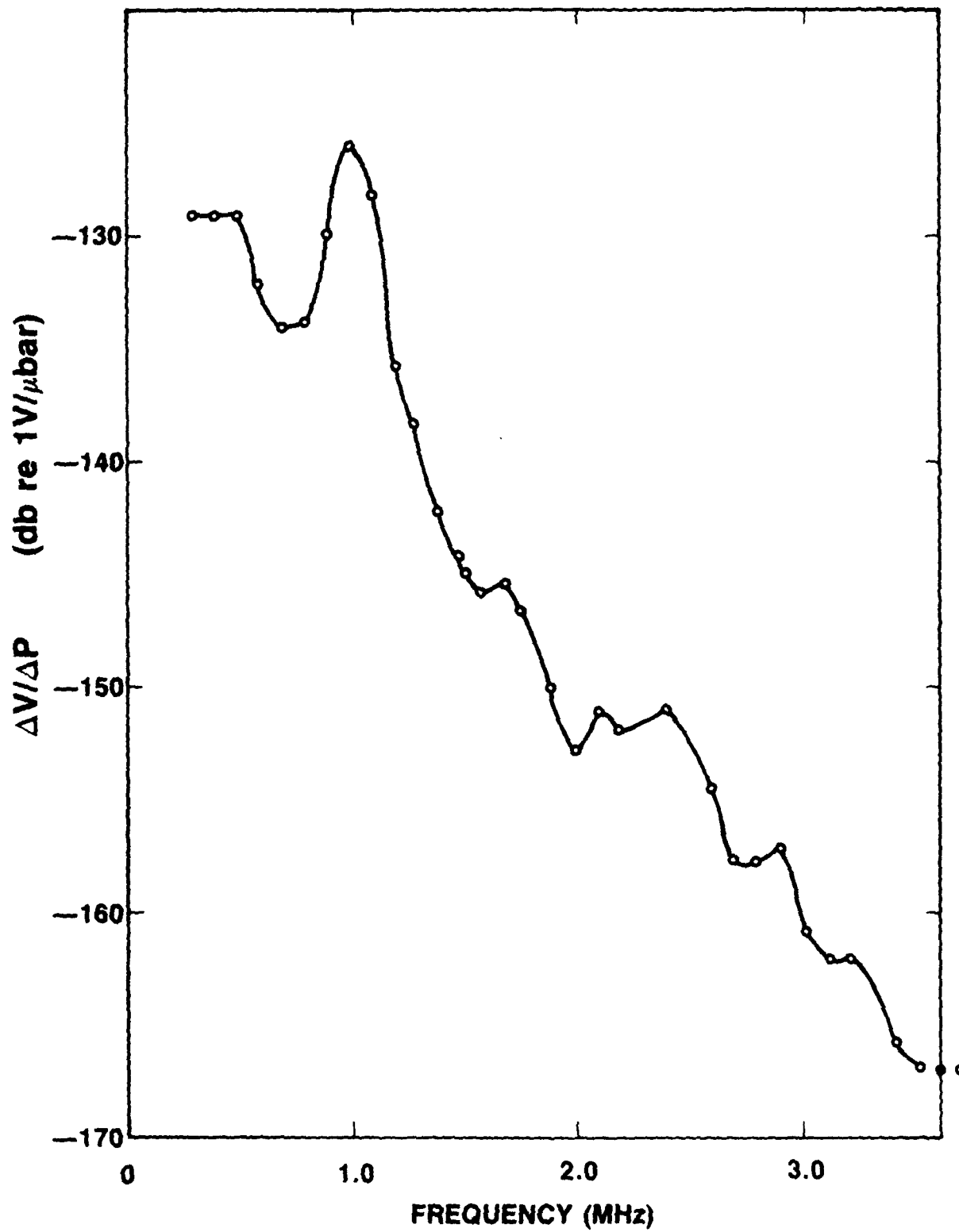


Figure A7

ACOUSTIC SENSITIVITY OF FIBER OPTIC COIL SENSOR

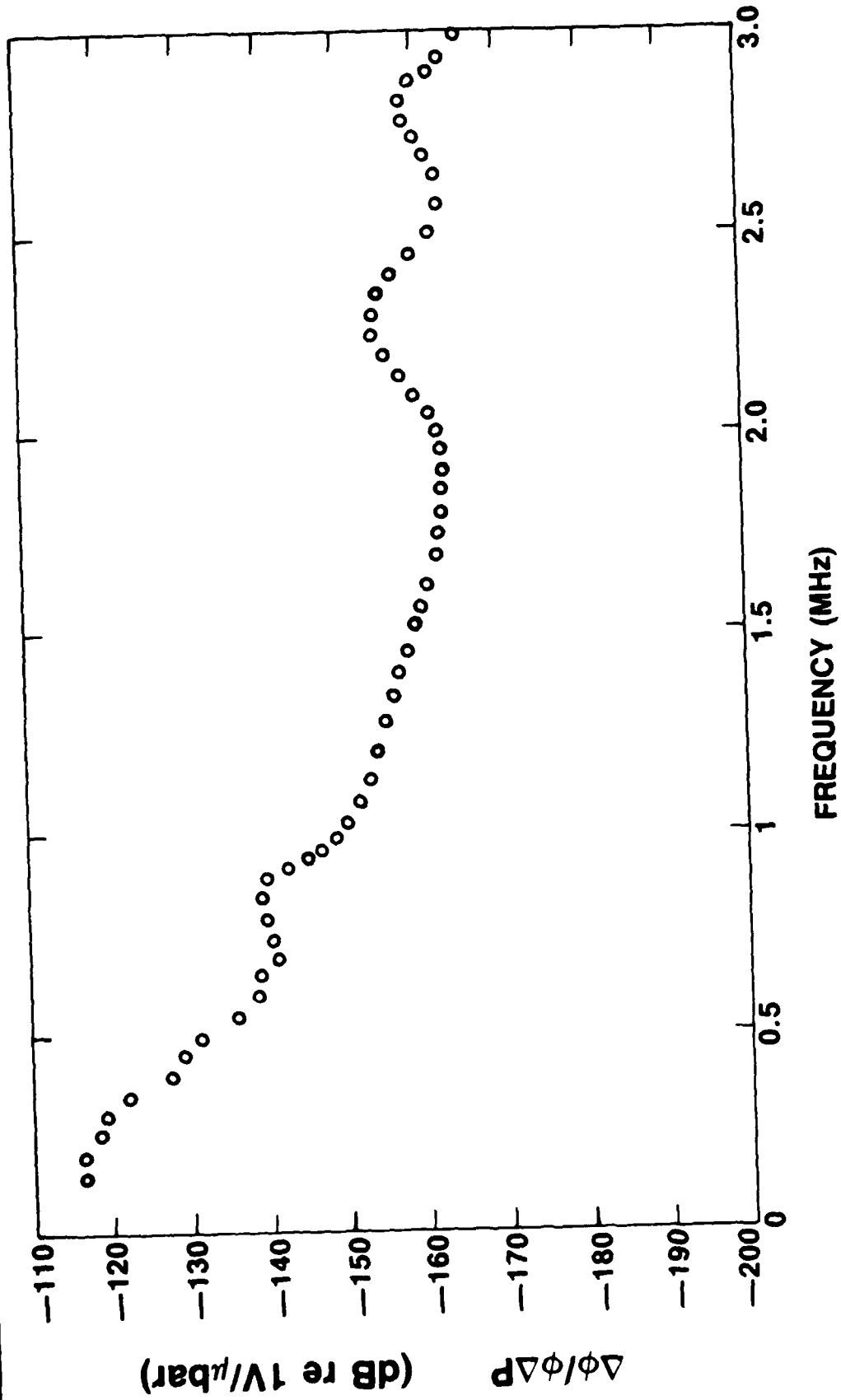
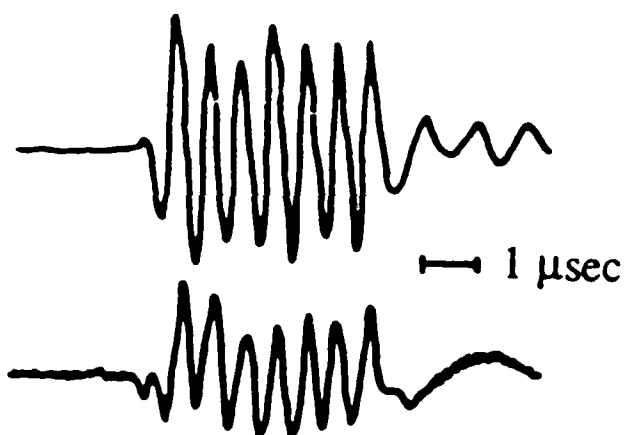


FIGURE A8

Response



Conventional
Probe

Fiber Optic
Probe

FIGURE A9

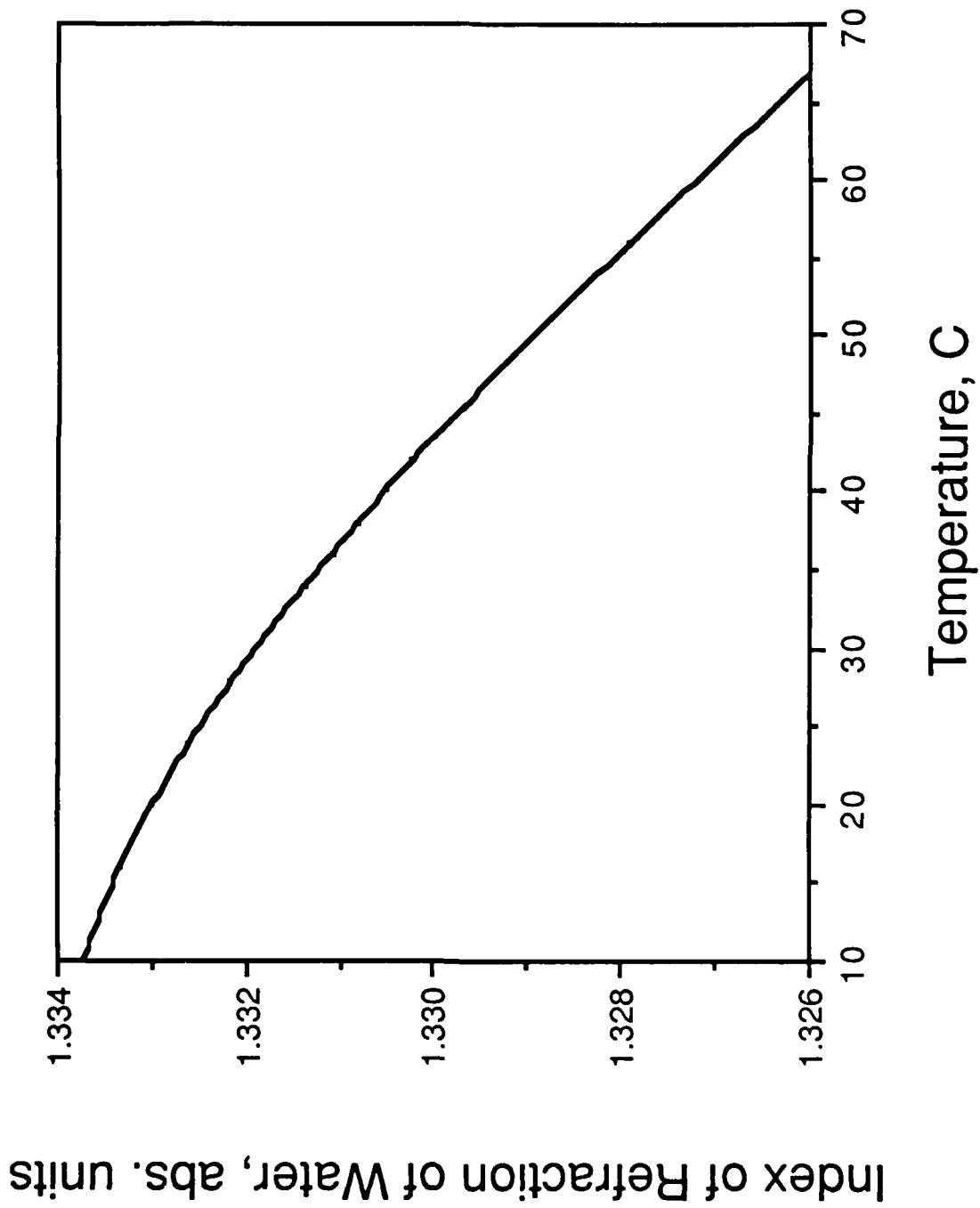
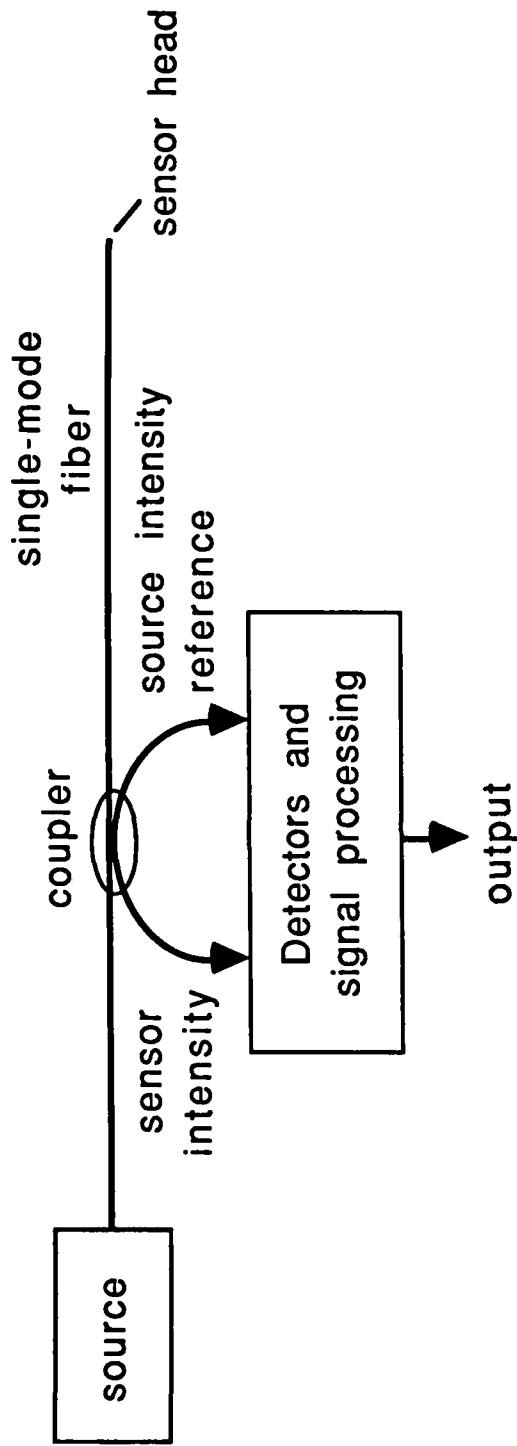
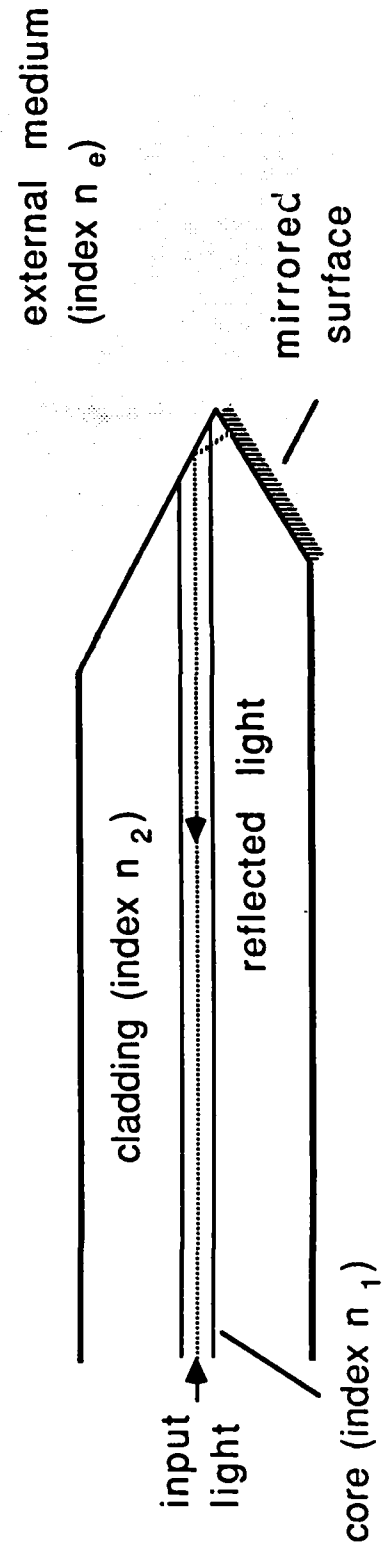


FIGURE A10

Sensor configuration



Probe head



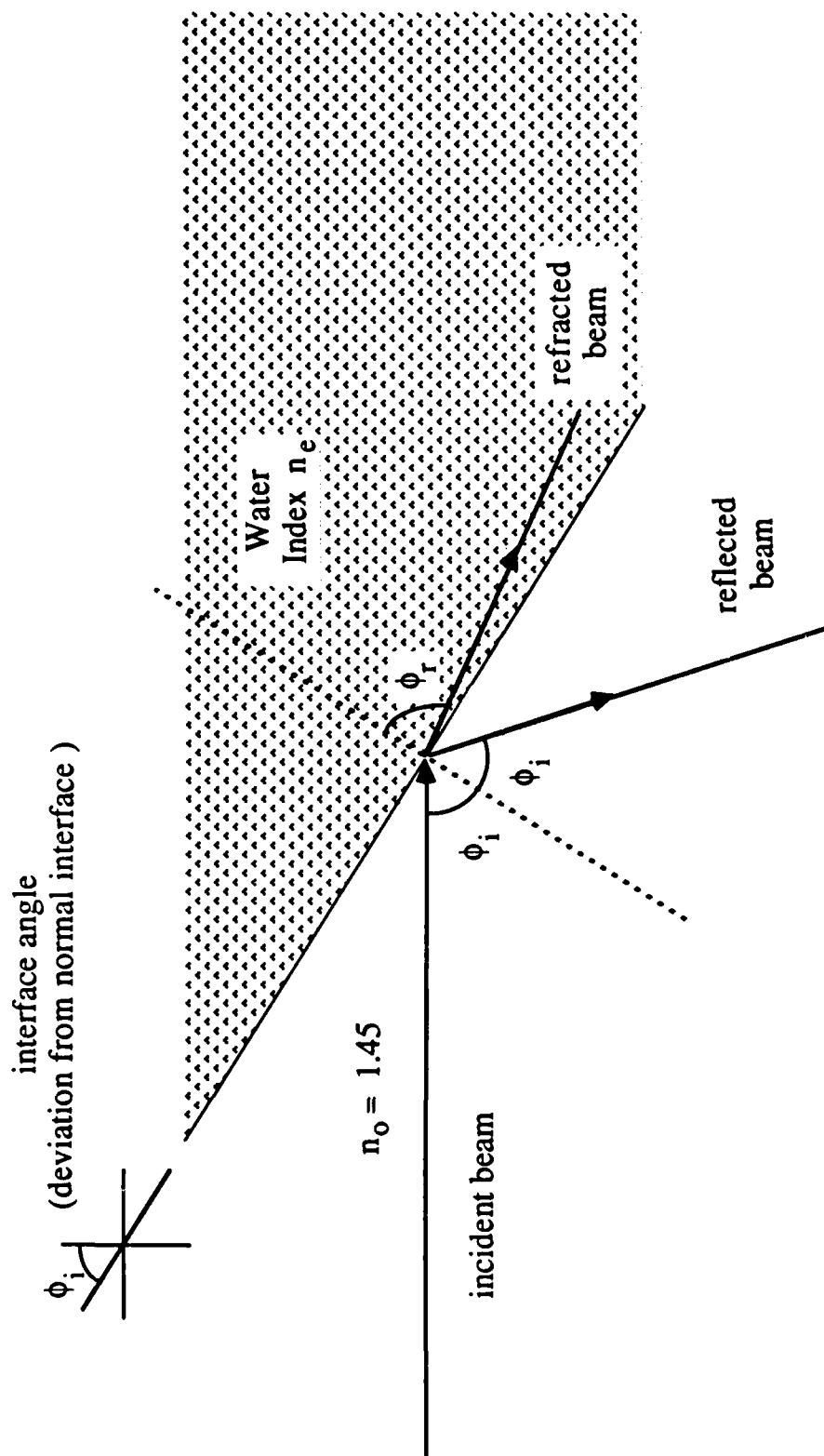


FIGURE A12

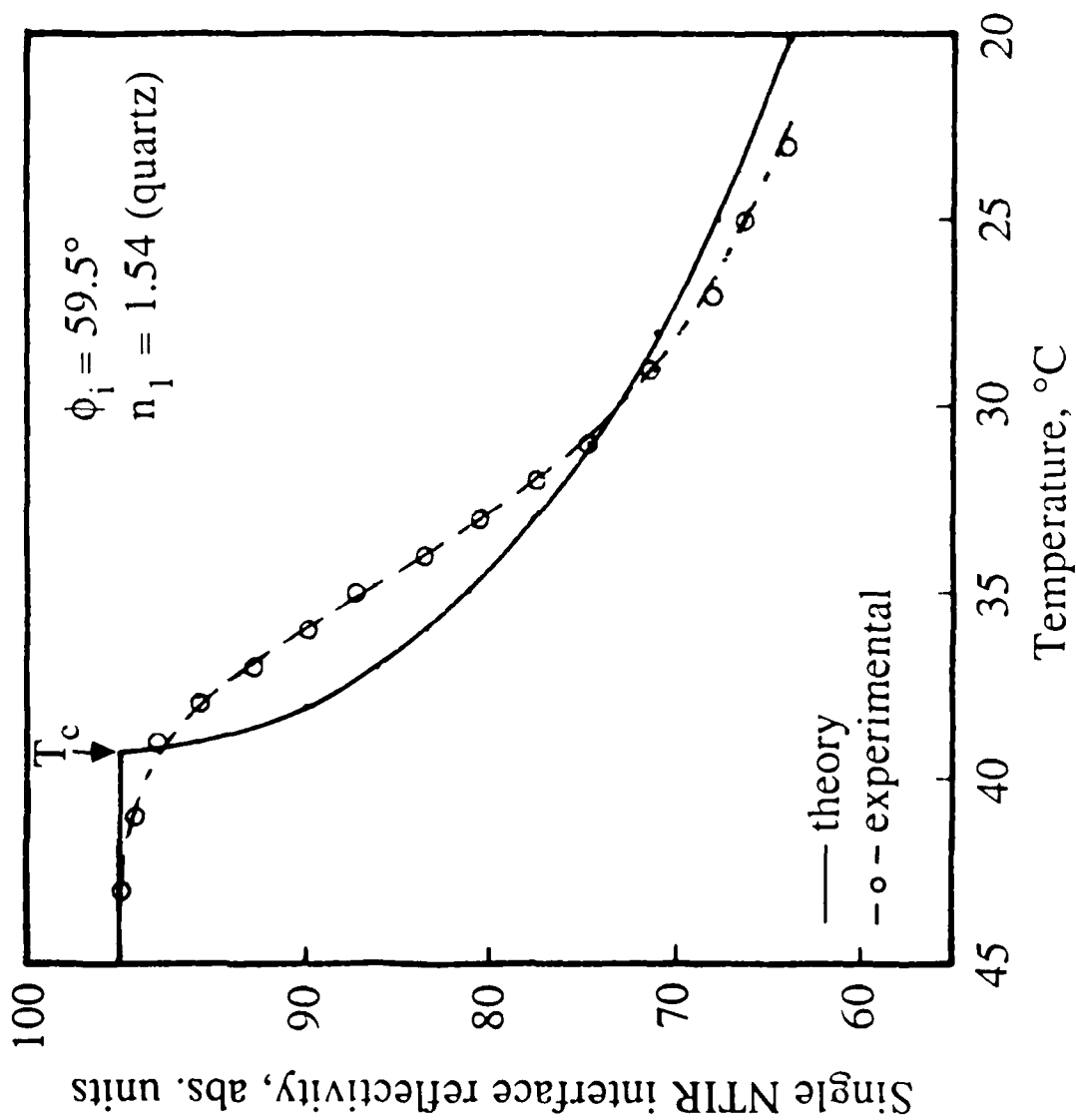


FIGURE A13

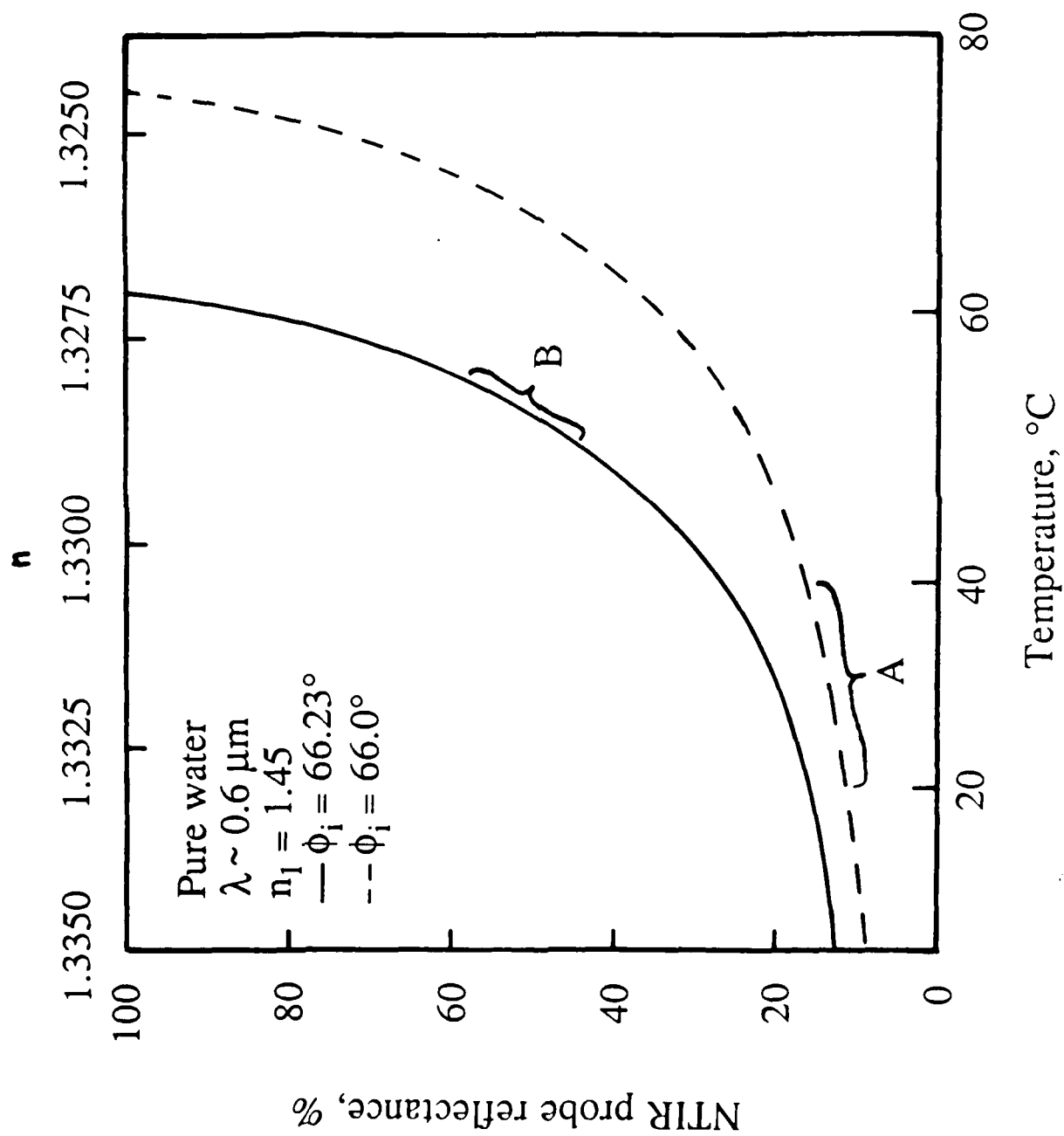
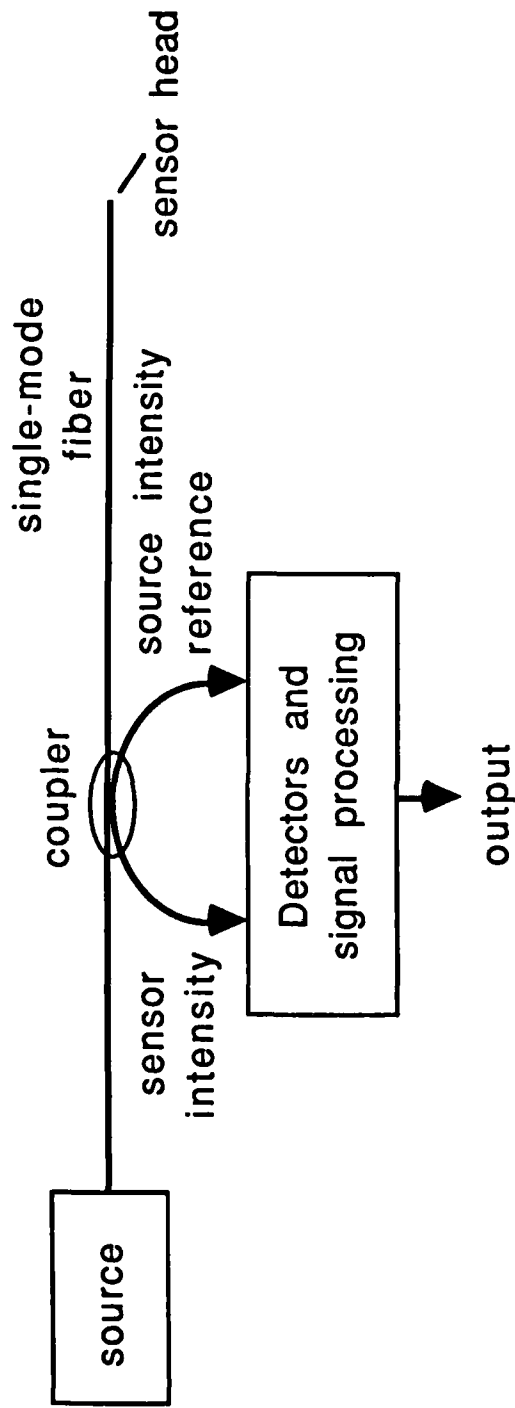
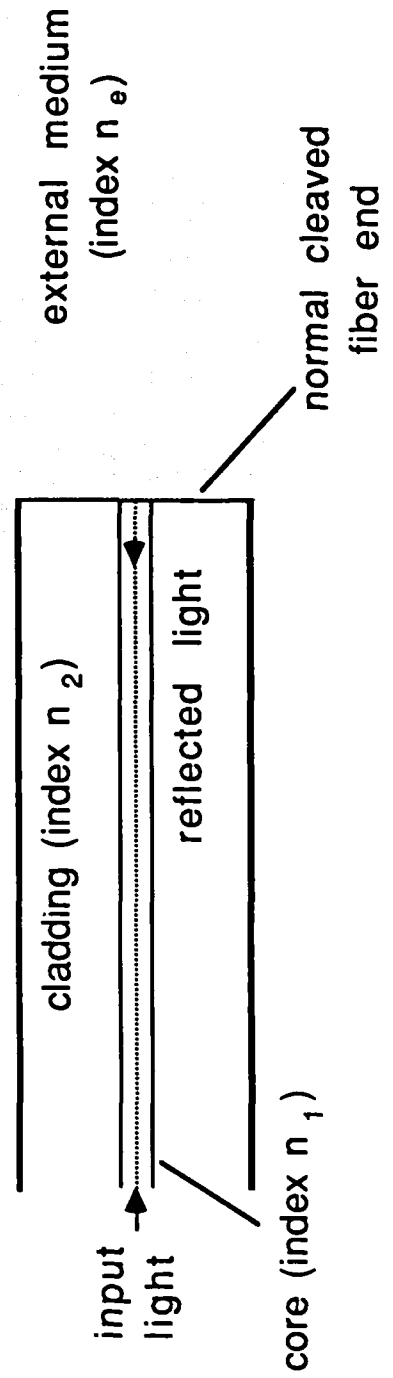


FIGURE A14

Sensor configuration



Probe head



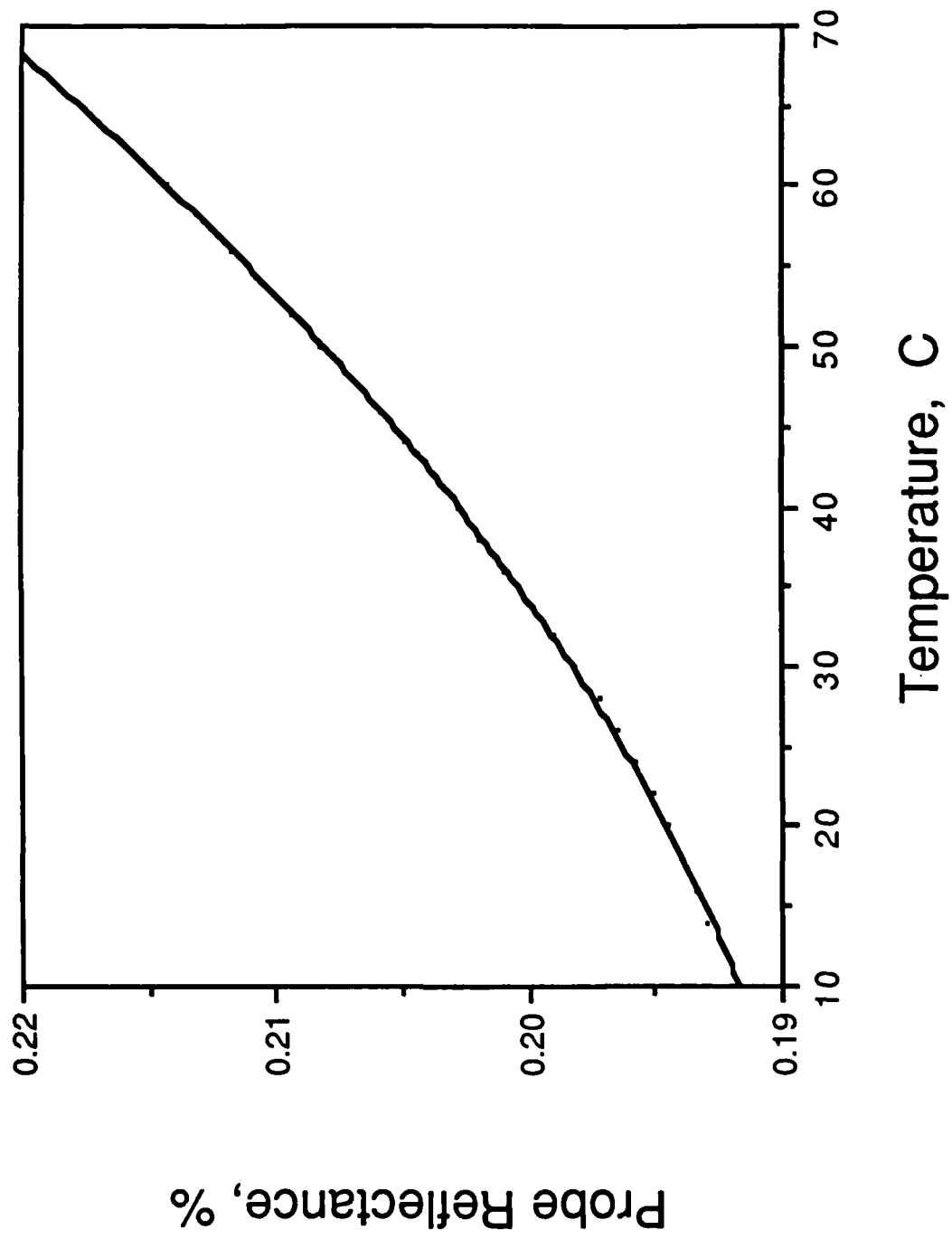


FIGURE A16

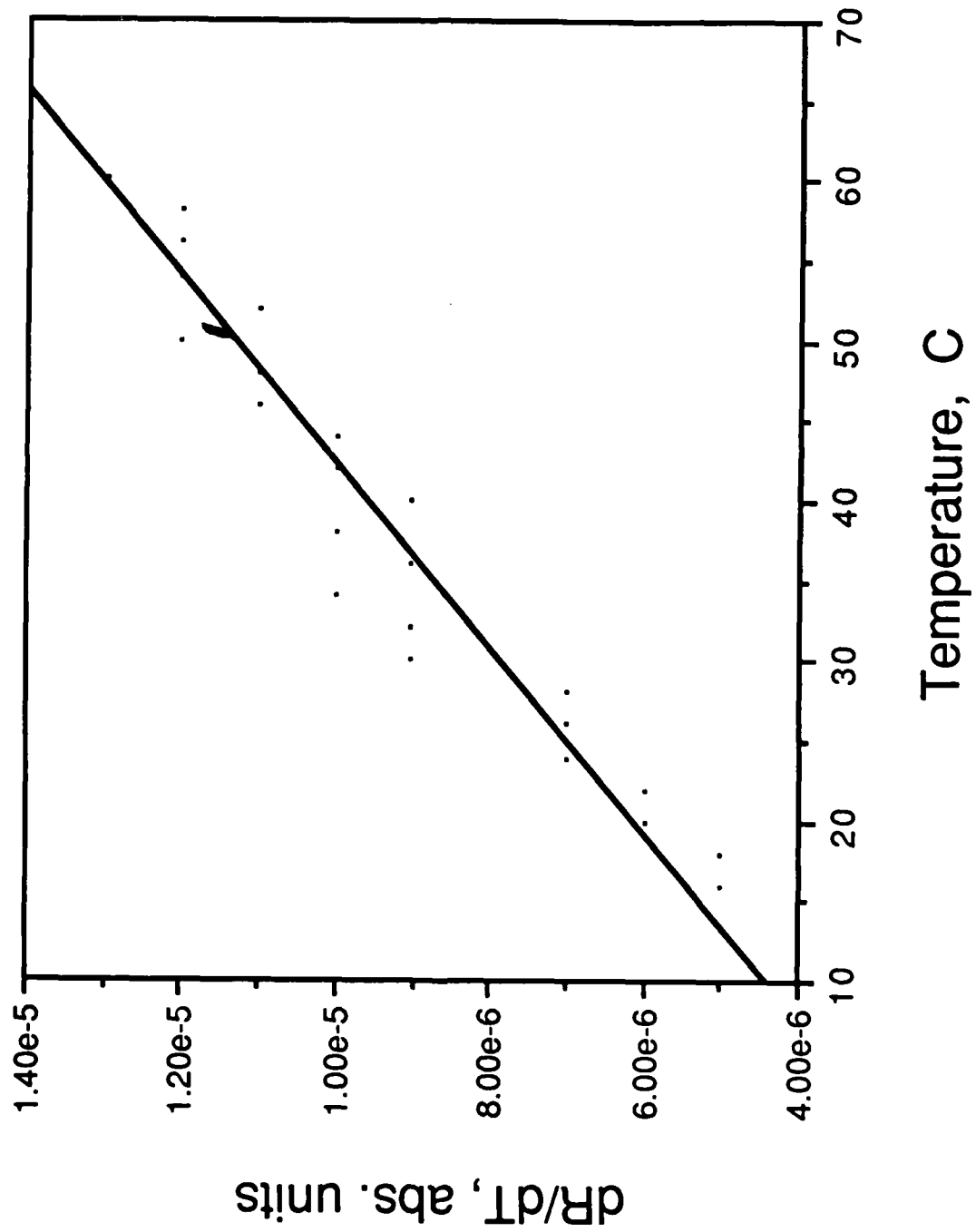


FIGURE A17

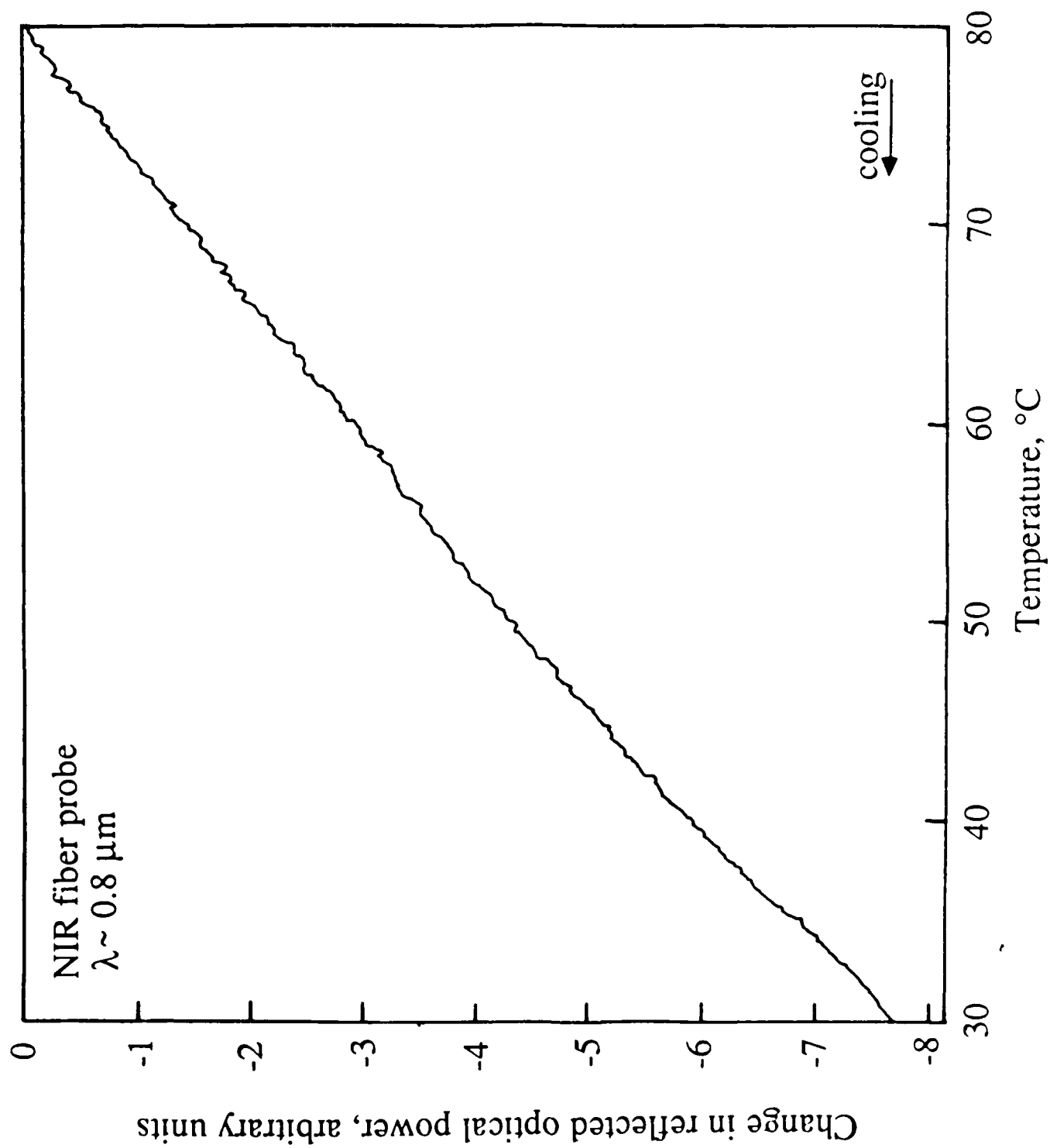


FIGURE A18

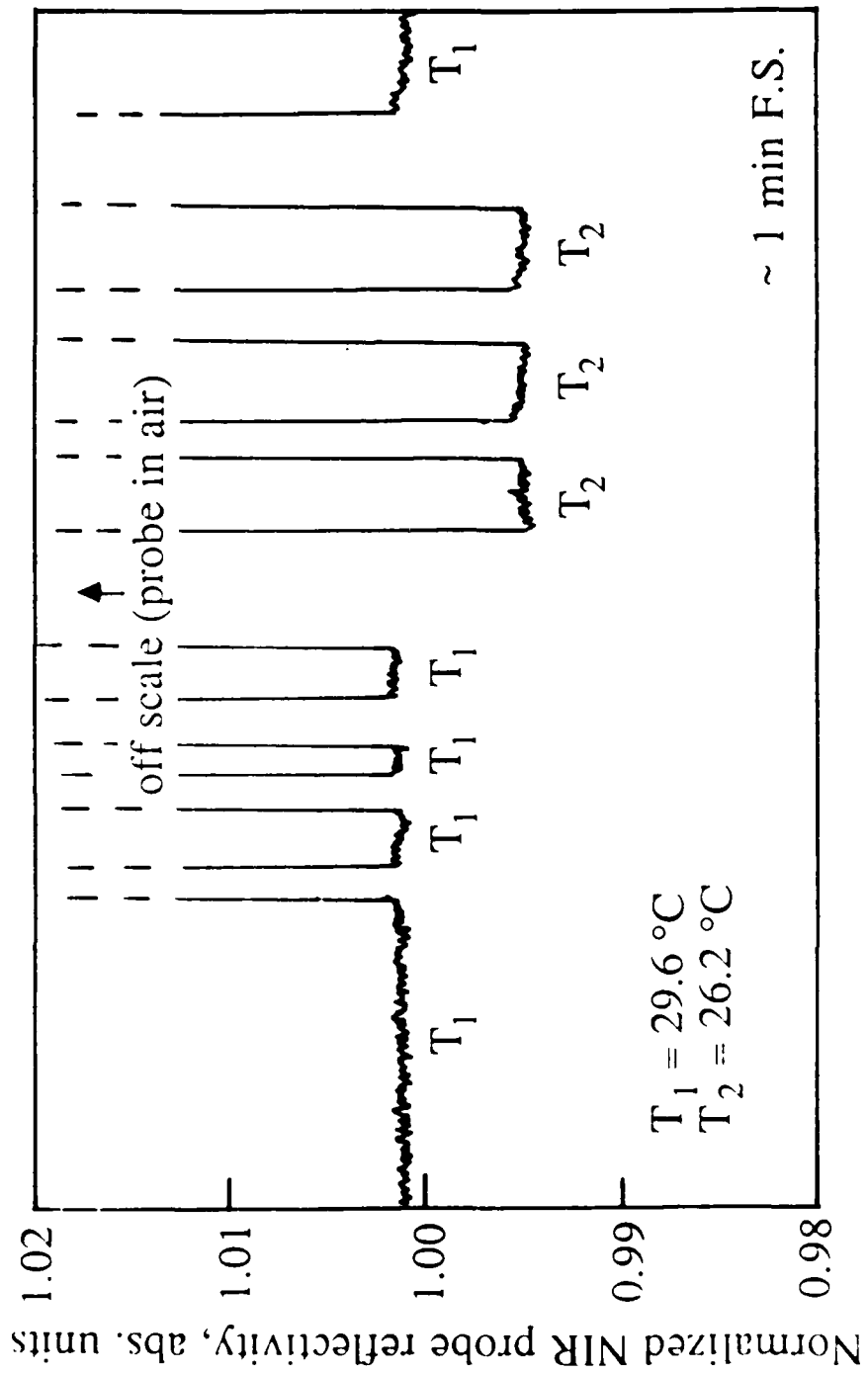


FIGURE A19

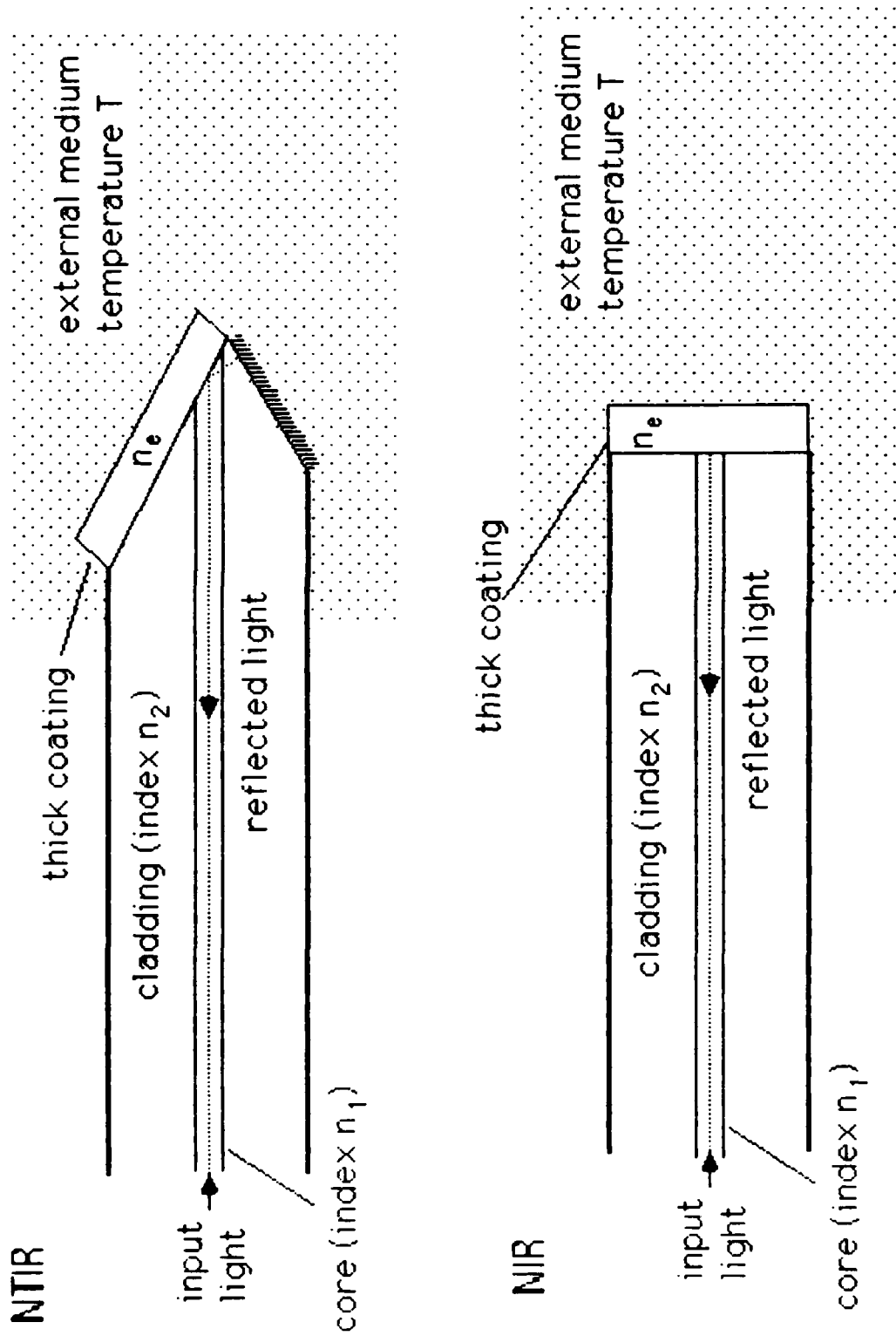


FIGURE A20

FIGURE CAPTIONS - Section B

- Figure B.1: Pulsed microwave setup used to test the fiber-optic pressure sensor (Walter Reed)
- Figure B.2: Interferometric output showing phase-to-intensity conversion at linear point on transfer function
- Figure B.3: Recorded sensor output due to pulsed microwave induced pressure transients in water sample
- Figure B.4: Output observed with sample cell walls lined with acoustically absorbing foam (note strong attenuation of high frequency ringing component c.f. Fig. B.3)
- Figure B.5: Pulsed microwave setup used to test the NIR fiber-optic temperature sensor
- Figure B.6: Transient temperature response due to a 10 μ s, 50 kw peak microwave pulse incident on water sample (note change in temperature $\sim 0.18^\circ\text{C}$, response time determined by electronics)
- Figure B.7: Temperature sensor response over ~ 8 sec. Microwave pulse at $t = 1$ sec, $\Delta T = 0.18^\circ\text{C}$

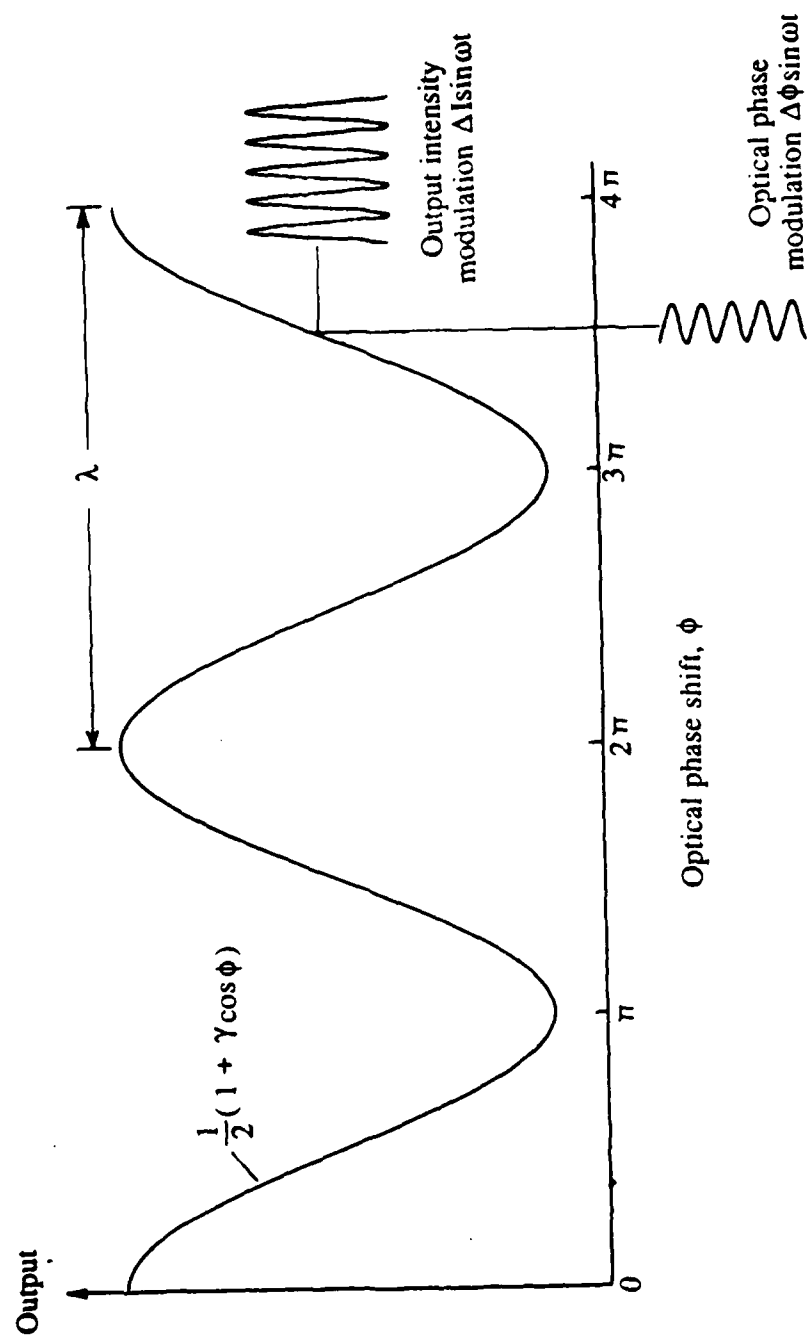
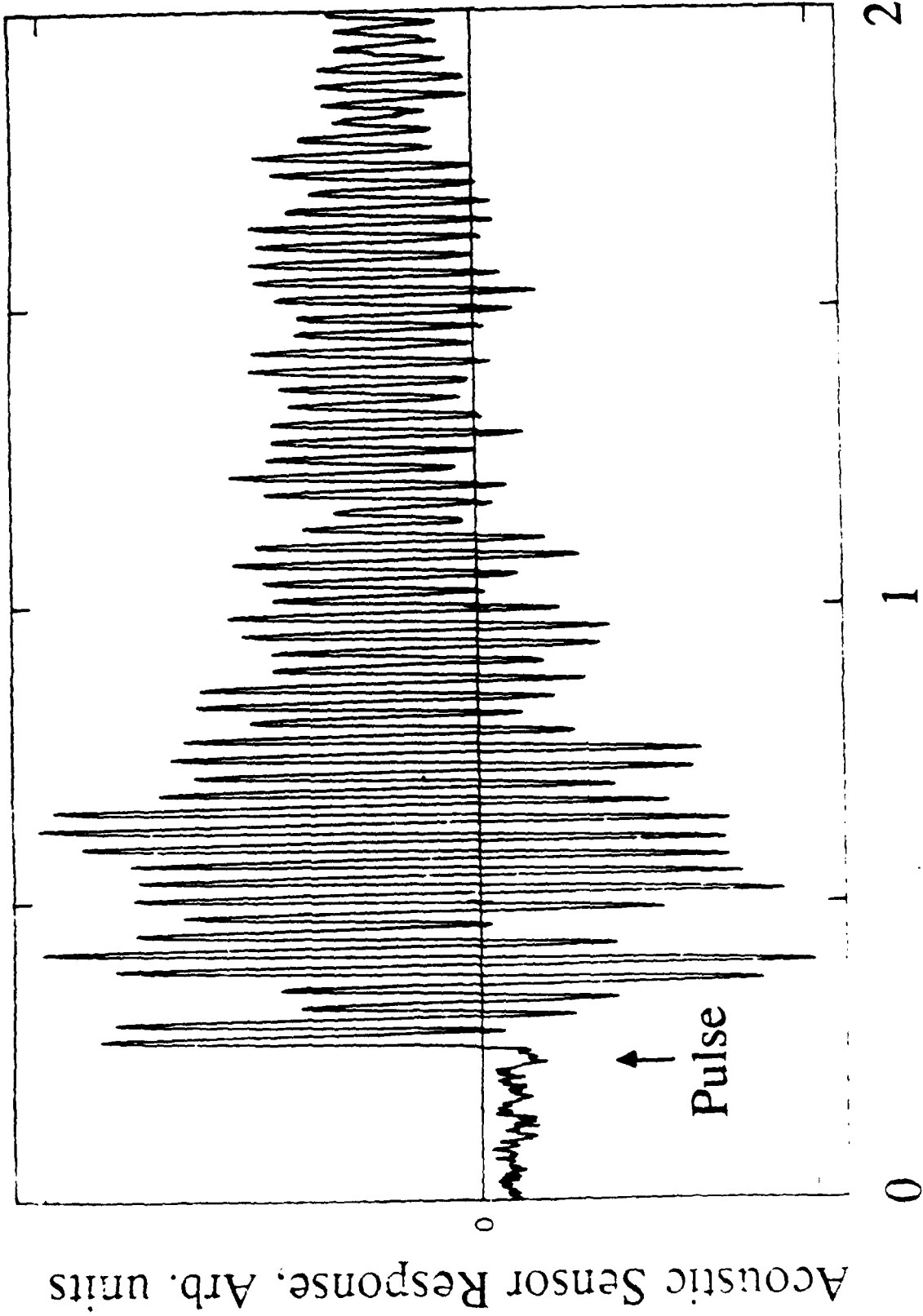


FIGURE B2

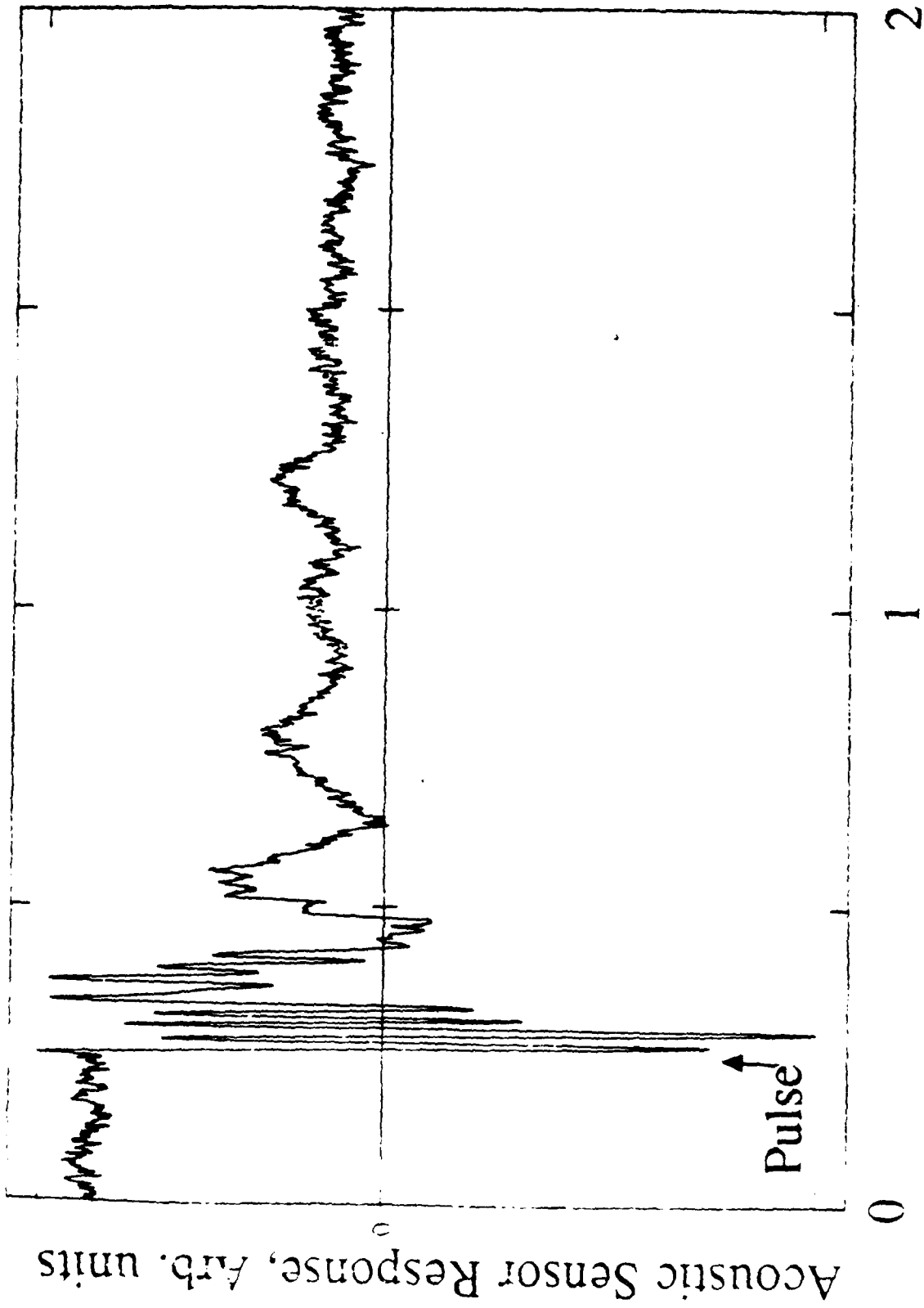
Pulsed-Microwave induced Pressure transient in
Water Sample: Undamped Chamber



Time, millisec.

FIGURE B3

Pulsed-Microwave induced Pressure Transient in Water Sample: Damped Chamber



Time, millisecond.

FIGURE B4

PULSED-MICROWAVE INDUCED TEMPERATURE TRANSIENTS IN WATER SAMPLE

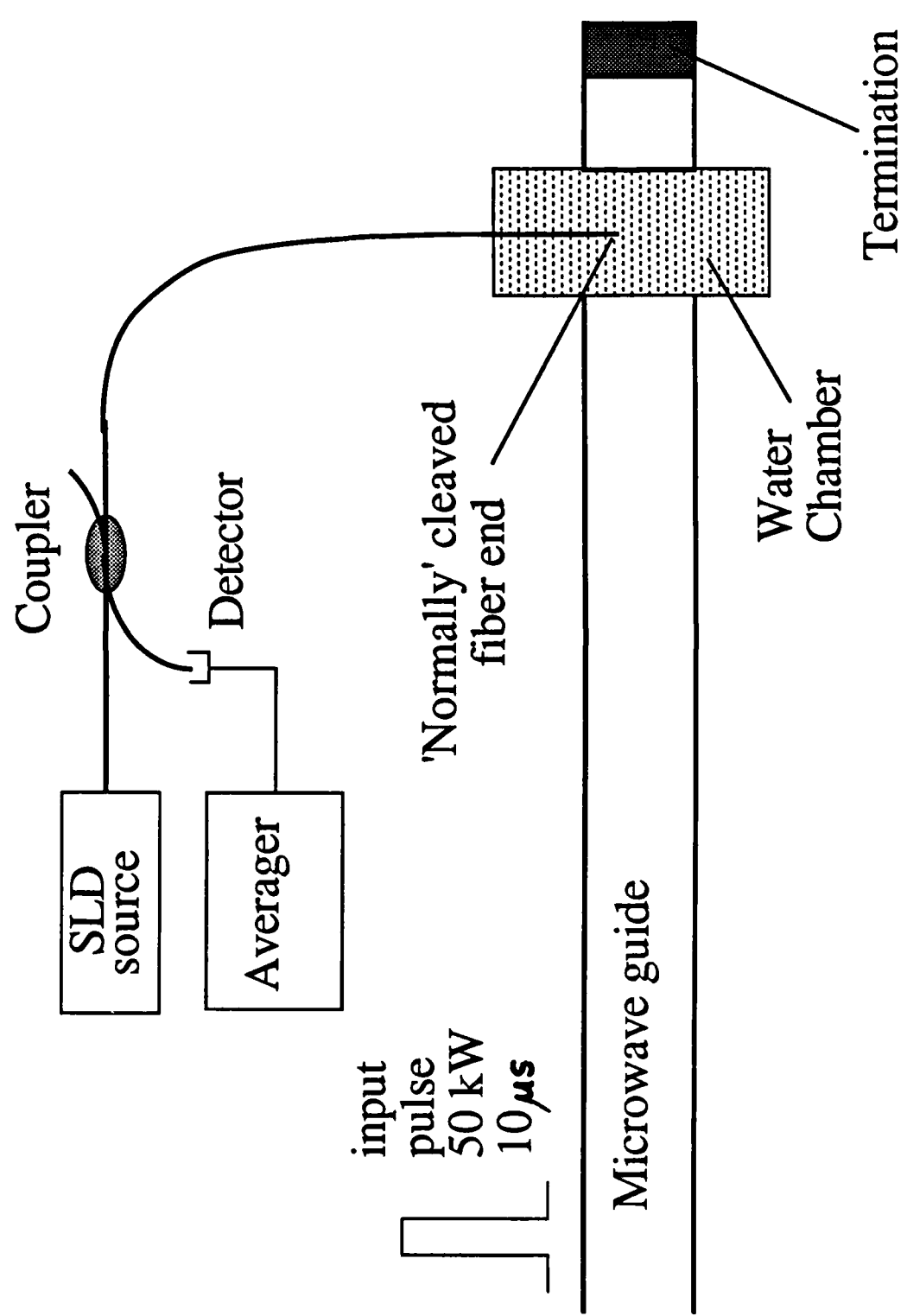
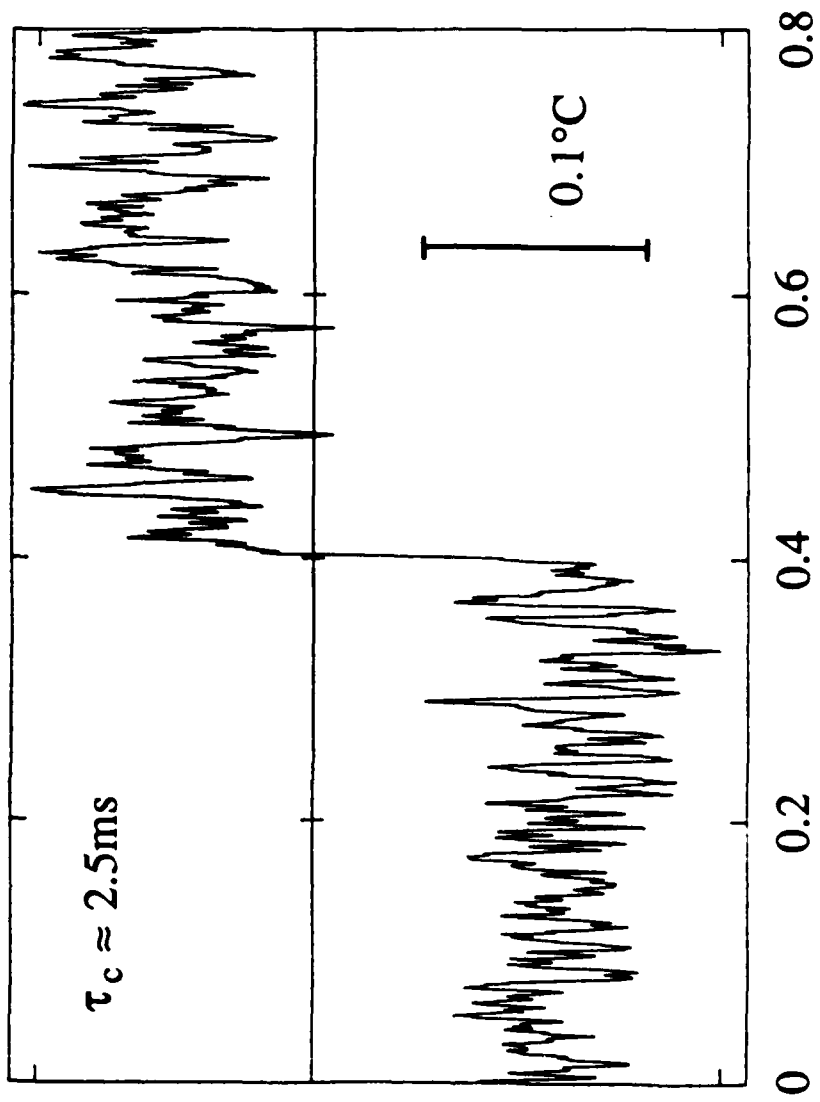


FIGURE B5

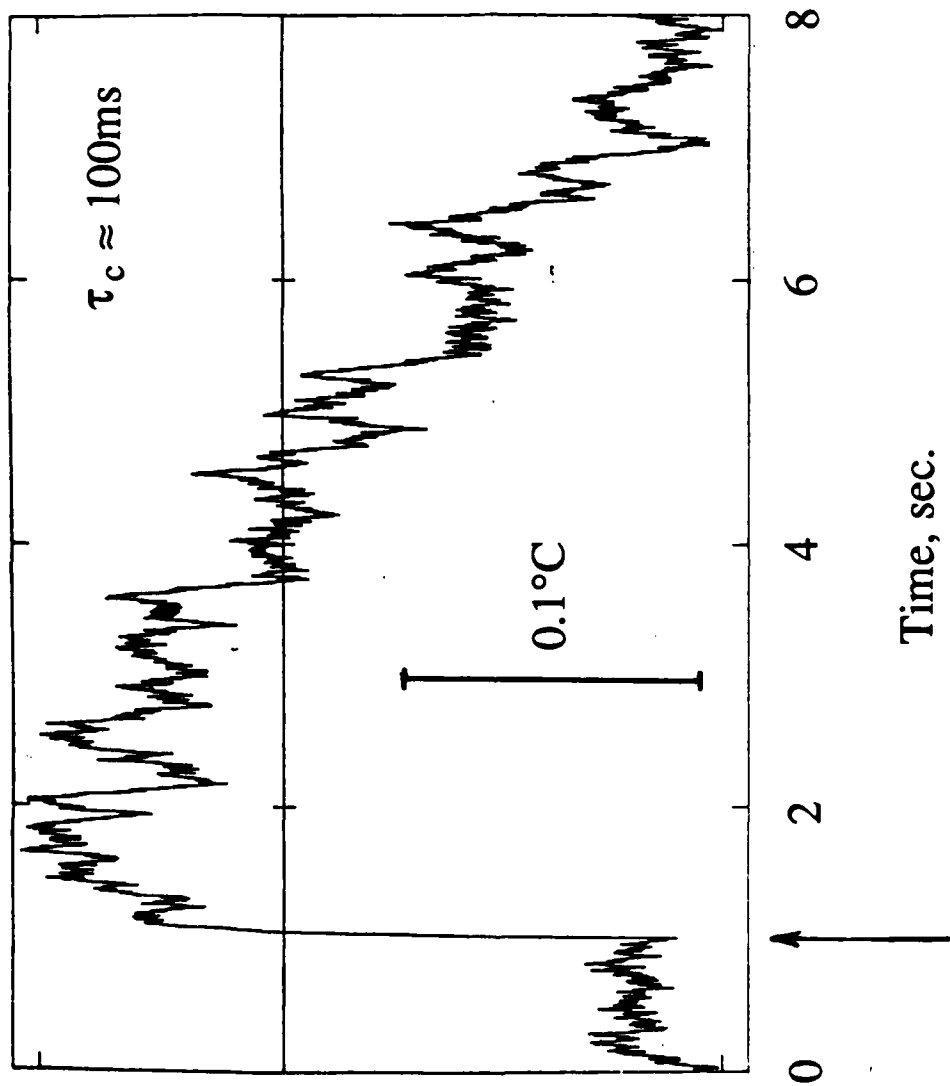


Time, sec.



50kW Peak 10 μ s
Microwave pulse

FIGURE B6



50kW Peak 10 μs
 Microwave pulse

FIGURE B7

FIGURE CAPTIONS - Section C

- Figure C.1: Layout of the prototype fiber-optic Mach-Zehnder interferometer pressure sensor for delivery to Walter Reed
- Figure C.2: Block diagram showing the demodulation electronics used in the pressure sensor
- Figure C.3: Schematic of the NIR temperature sensor and electronics
- Figure C.4: Typical spectrum of the type of SLD used to power the NIR temperature sensor (note wide bandwidth reduces interfering coherence effects in the intensity based sensor)
- Figure C.5: NIR temperature sensor output drift without (a) and with (b) source intensity stabilization
- Figure C.6: Sensor output stability over a 2 min period
- Figure C.7: Fiber optic NIR temperature sensor: front panel
- Figure C.8: Fiber optic NIR temperature sensor: rear panel
- Figure C.9: SLD power supply: front panel
- Figure C.10: SLD power supply: rear panel

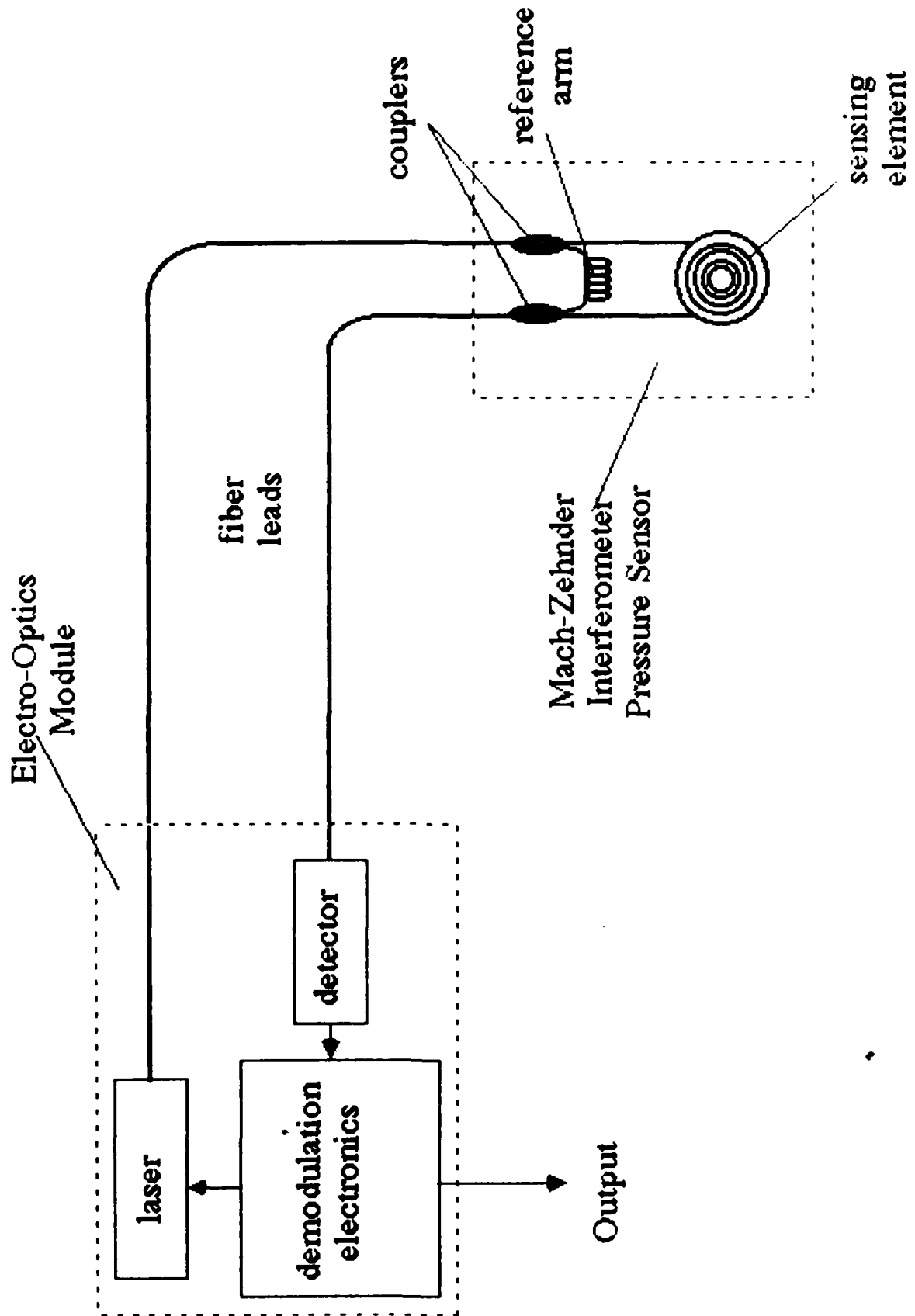
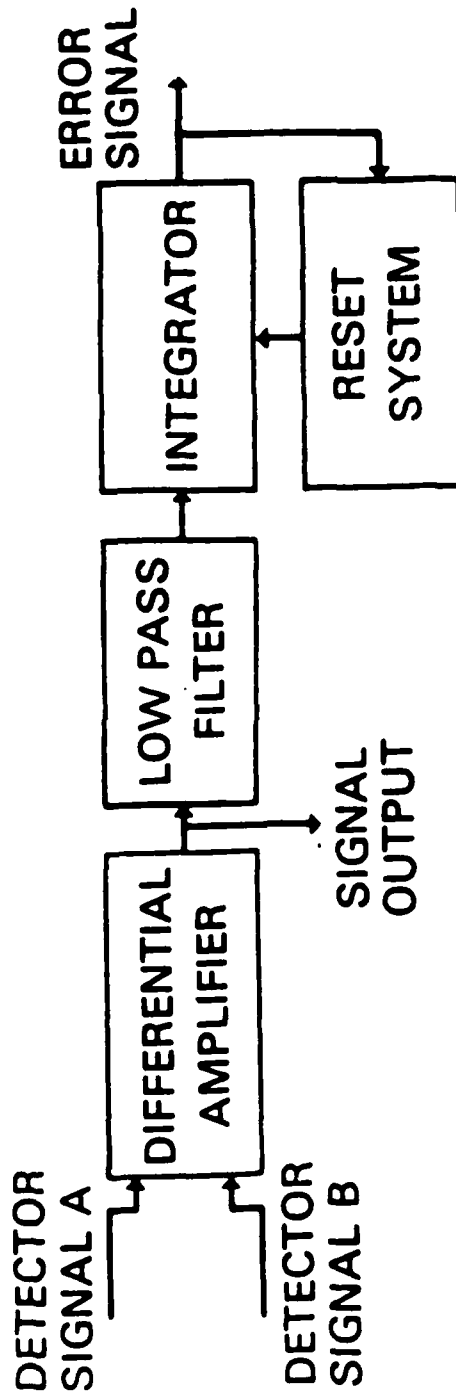


FIGURE C1

Demodulation Approach



Fiber-Optic NIR Temperature Sensor

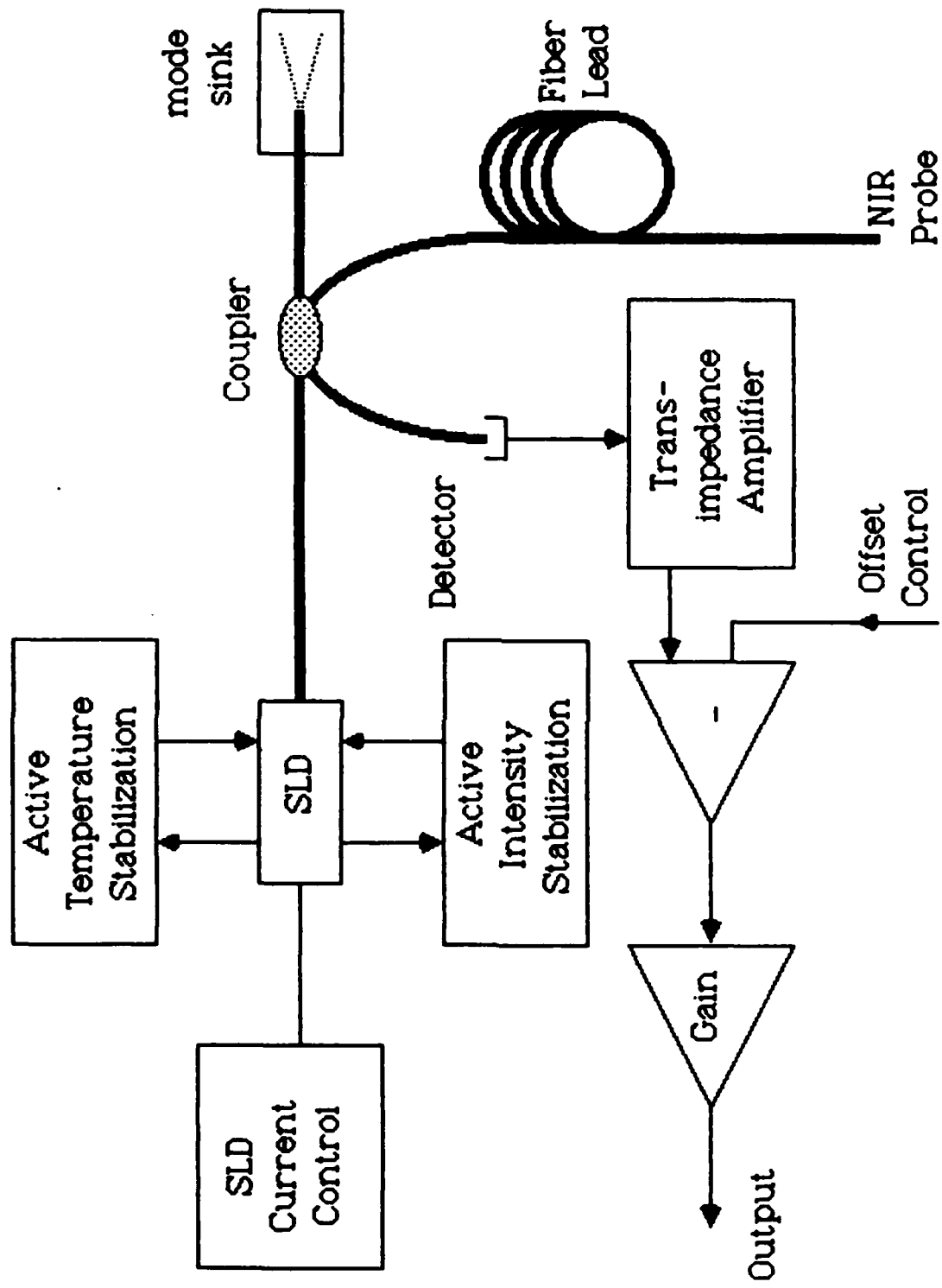


FIGURE C3

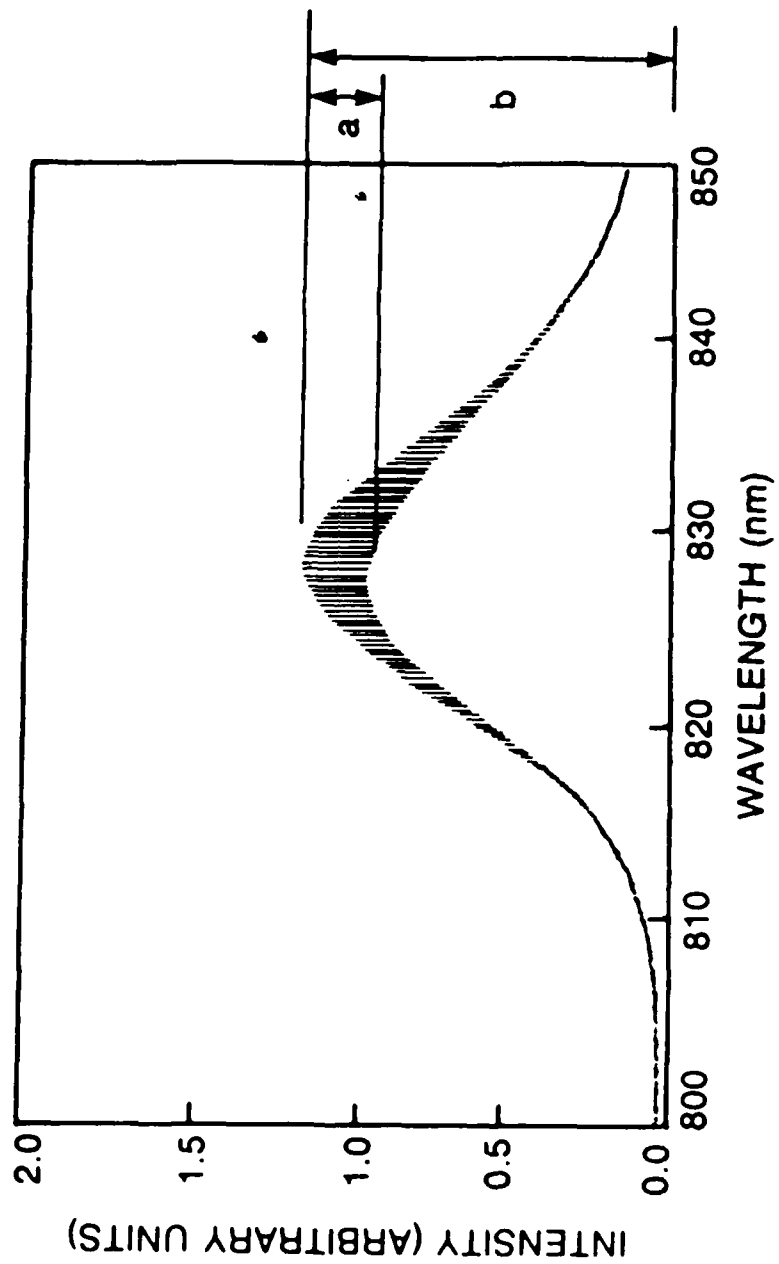


FIGURE C4

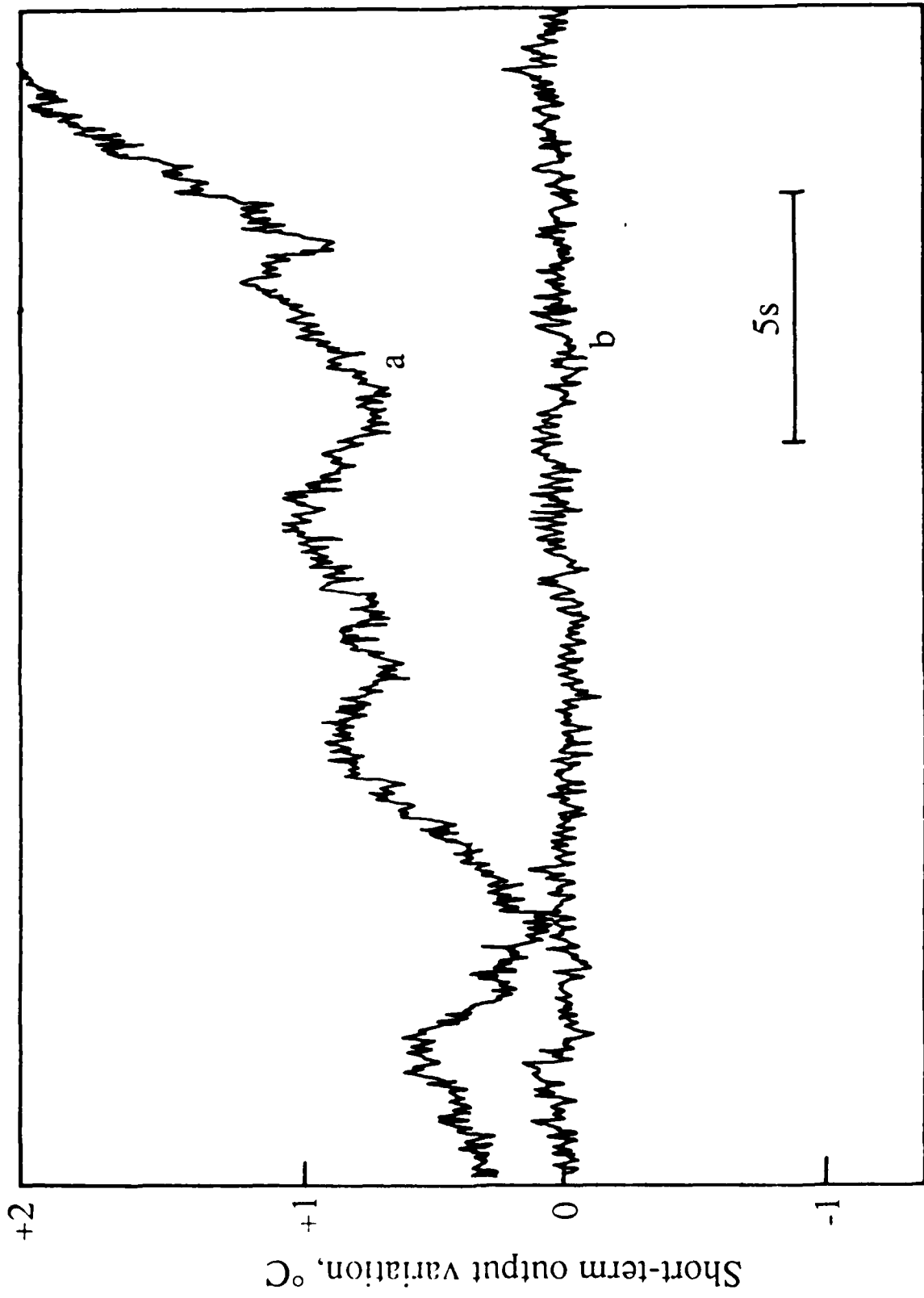


FIGURE C5

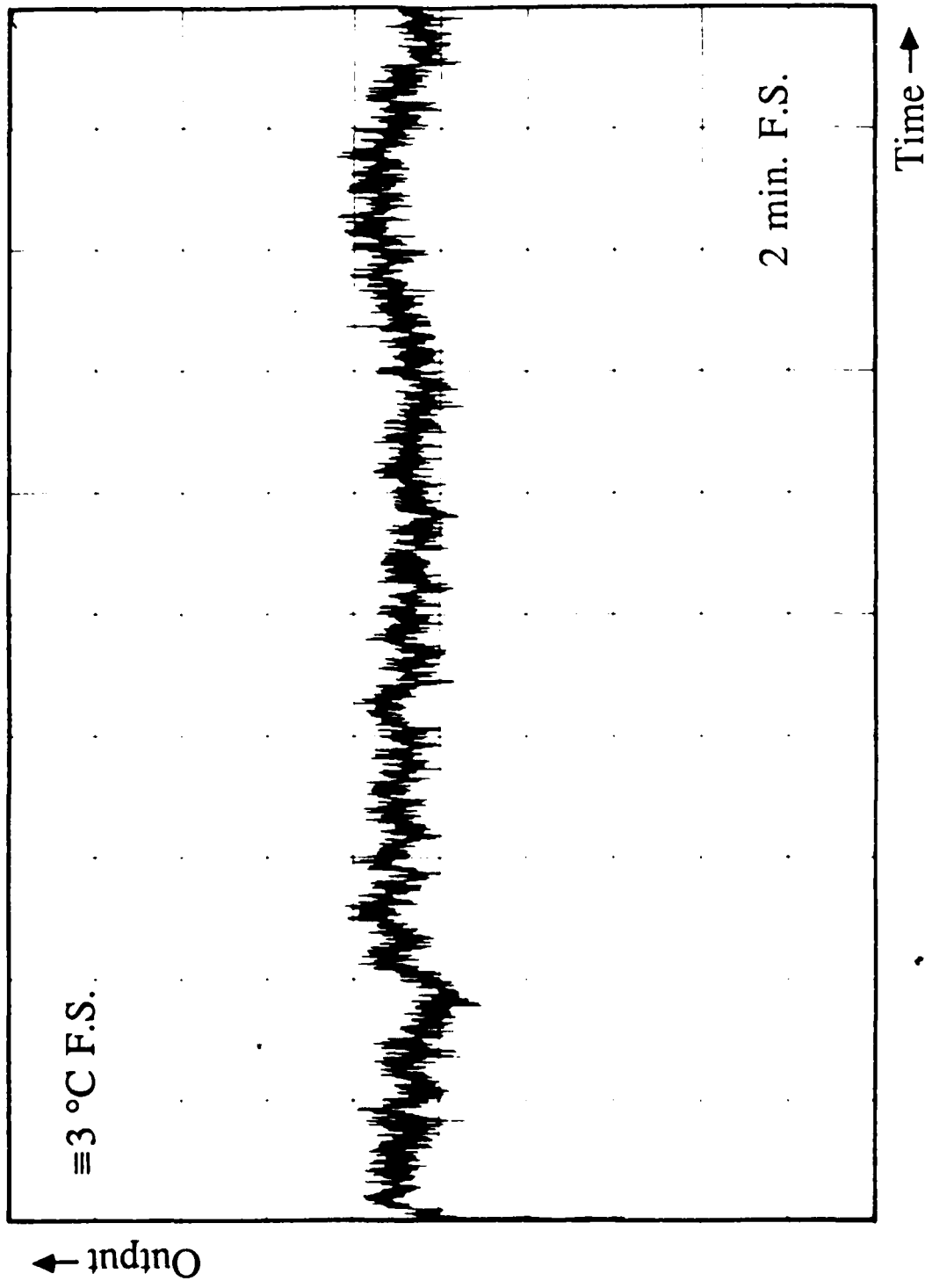
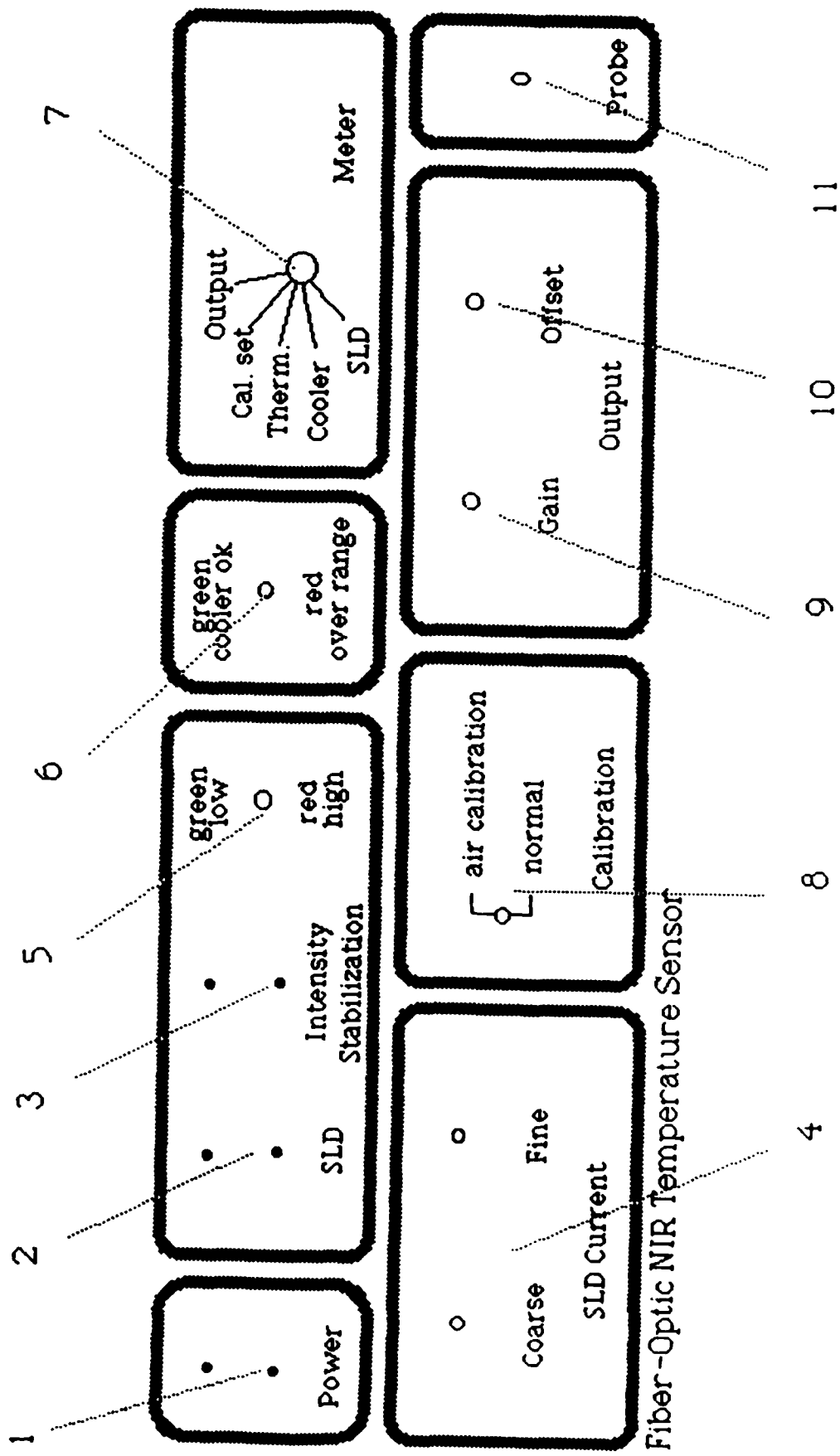
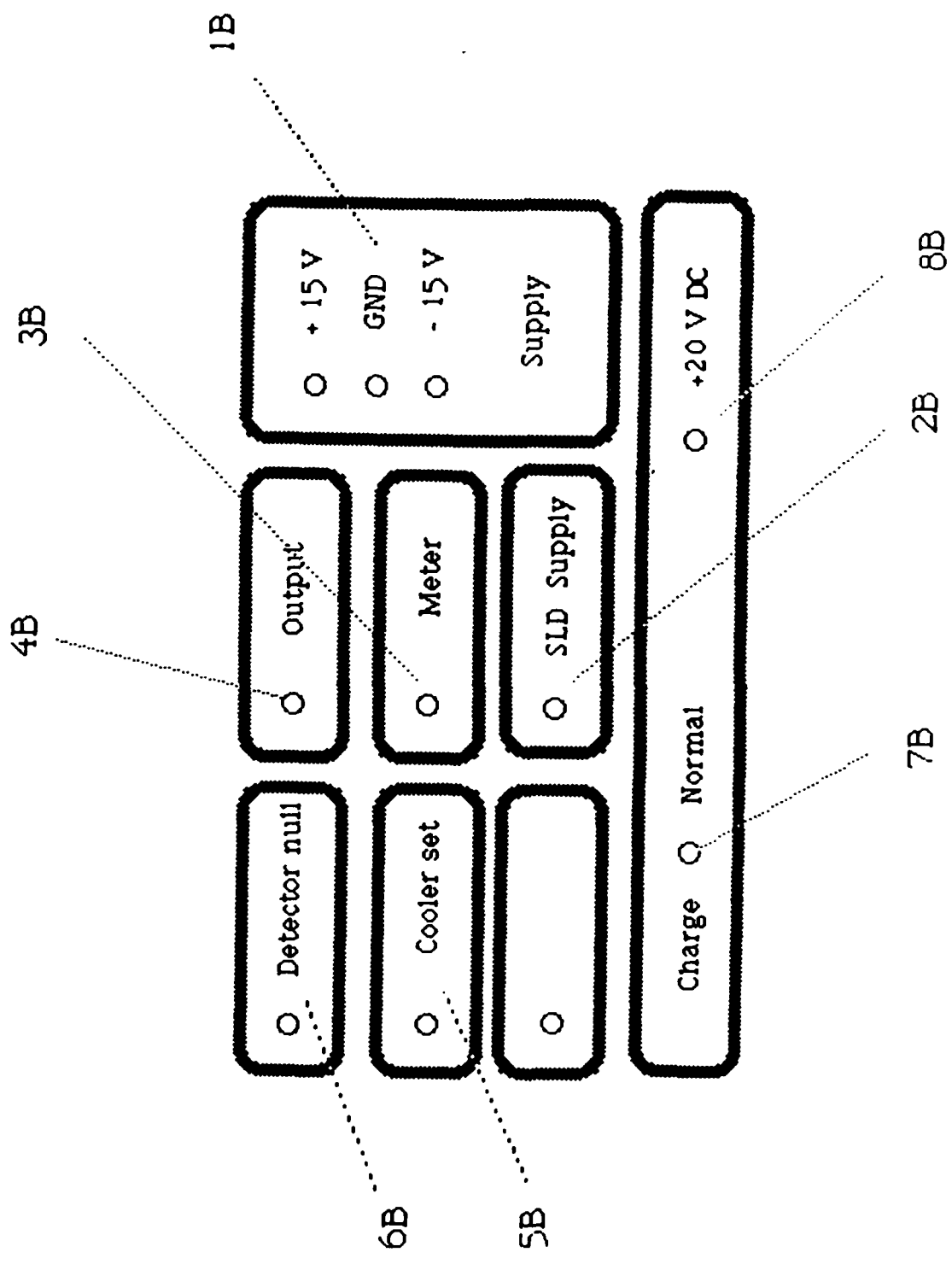


FIGURE C 6



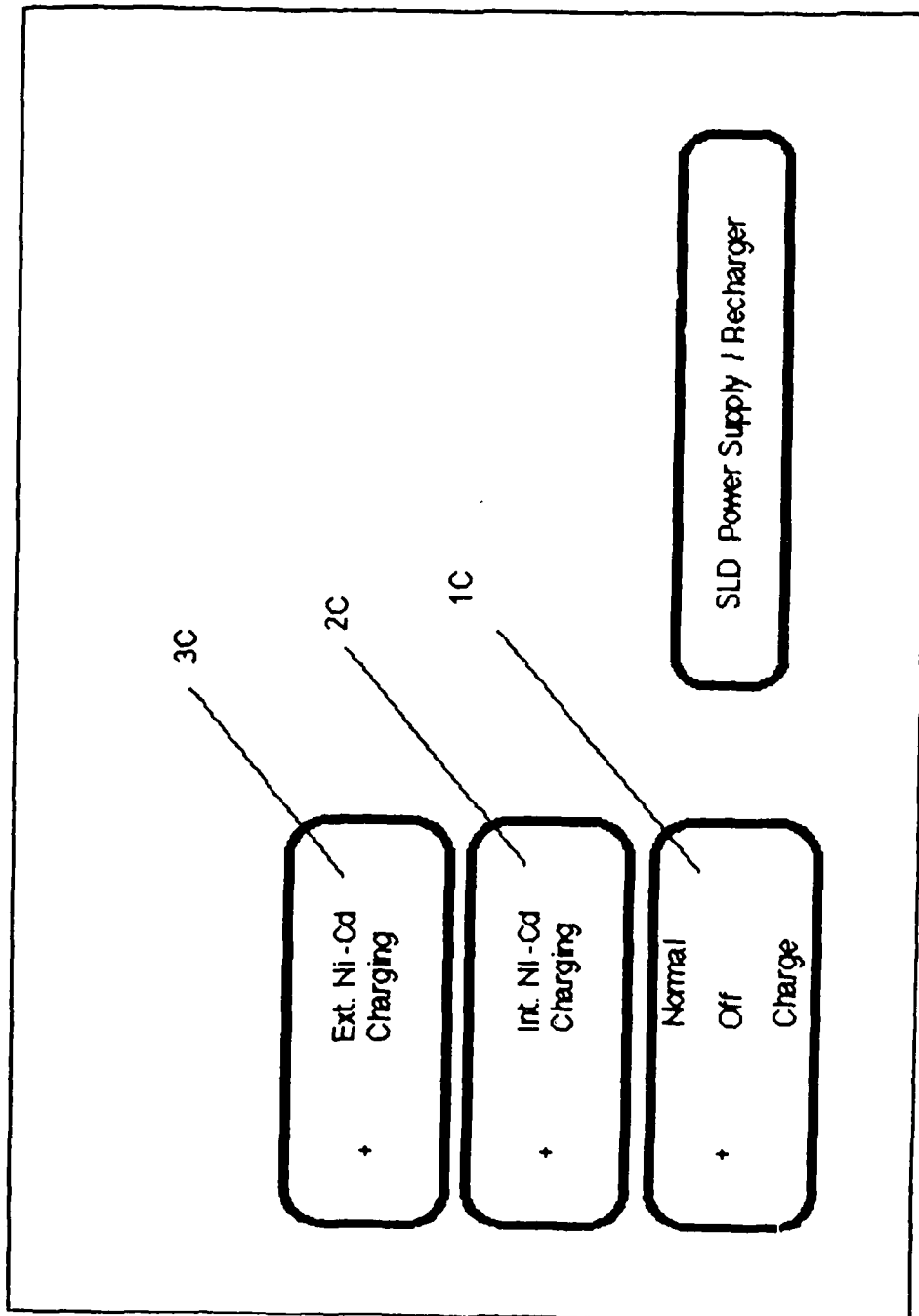
Fiber-Optic NIR Temperature Sensor: Front Panel

FIGURE C7



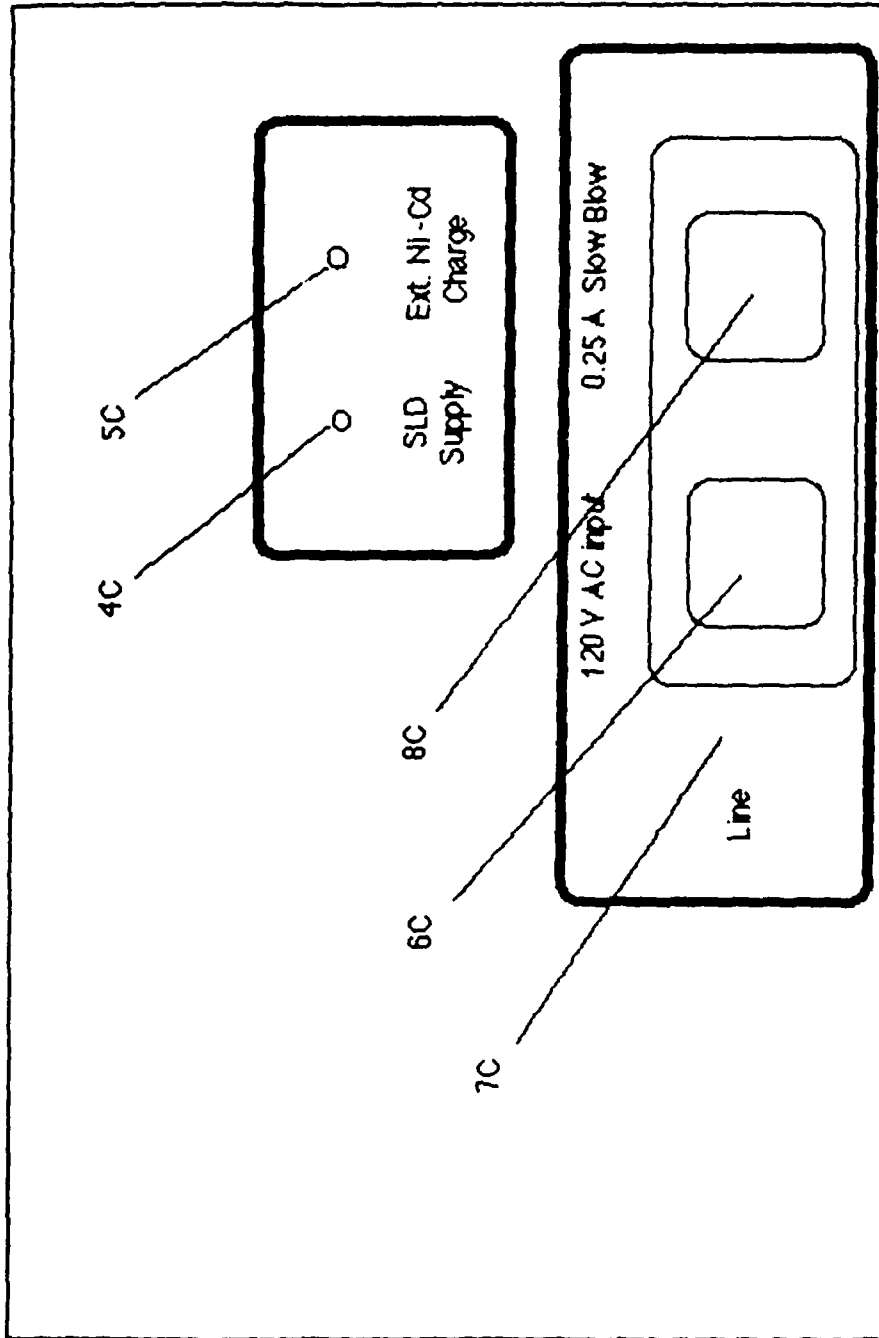
Fiber-Optic NIR Temperature Sensor: Rear Panel

FIGURE C8



SLD Power Supply/Recharger: Front Panel

FIGURE C9



SLD Power Supply/Recharger: Rear Panel

FIGURE C10

END

3-88

DTIC